AFRL-SN-RS-TR-2001-153
Final Technical Report
August 2001

MULTI-DIMENSIONAL INTERFERENCE REJECTION & TARGET DETECTION IN EARLY WARNING AIRBORNE RADAR

Research Associates for Defense Conversion, Inc.

Raviraj S. Adve

APPROVED FOR PUBLIC RELEASE; DISTRIBUTION UNLIMITED.

AIR FORCE RESEARCH LABORATORY
SENSORS DIRECTORATE
ROME RESEARCH SITE
ROME, NEW YORK

Although this report references limited documents (*), listed on page 63, no limited information has been extracted.

This report has been reviewed by the Air Force Research Laboratory, Information Directorate, Public Affairs Office (IFOIPA) and is releasable to the National Technical Information Service (NTIS). At NTIS it will be releasable to the general public, including foreign nations.

AFRL-SN-RS-TR-2001-153 has been reviewed and is approved for publication.

APPROVED:

DAVID B. BUNKER
Project Engineer

FOR THE DIRECTOR: Robert G. Polce

ROBERT G. POLCE, Chief
Rome Operations Office
Sensors Directorate

If your address has changed or if you wish to be removed from the Air Force Research Laboratory Rome Research Site mailing list, or if the addressee is no longer employed by your organization, please notify AFRL/SNRT, 26 Electronic Pky, Rome, NY 13441-4514. This will assist us in maintaining a current mailing list.

Do not return copies of this report unless contractual obligations or notices on a specific document require that it be returned.

REPORT DOCUMENTATION PAGE	*Form Approved* *OMB No. 0704-0188*

1. AGENCY USE ONLY *(Leave blank)*	2. REPORT DATE	3. REPORT TYPE AND DATES COVERED
	AUGUST 2001	Final Jan 97 - Oct 99

4. TITLE AND SUBTITLE
MULTI-DIMENSIONAL INTERFERENCE REJECTION & TARGET DETECTION IN EARLY WARNING AIRBORNE RADAR

5. FUNDING NUMBERS
C - F30602-97-C-0006
PE - 62204F
PR - 4506
TA - 11
WU - PF

6. AUTHOR(S)
Raviraj S. Adve

7. PERFORMING ORGANIZATION NAME(S) AND ADDRESS(ES)
Research Associates for Defense Conversion Inc.
10002 Hillside Terrace
Marcy New York 13403

8. PERFORMING ORGANIZATION REPORT NUMBER
N/A

9. SPONSORING/MONITORING AGENCY NAME(S) AND ADDRESS(ES)
Air Force Research Laboratory/SNRT
26 Electronic Parkway
Rome New York 13441-4514

10. SPONSORING/MONITORING AGENCY REPORT NUMBER
AFRL-SN-RS-TR-2001-153

11. SUPPLEMENTARY NOTES
Air Force Research Laboratory Project Engineer: David B. Bunker/SNRT/(315) 330-2345

12a. DISTRIBUTION AVAILABILITY STATEMENT
APPROVED FOR PUBLIC RELEASE; DISTRIBUTION UNLIMITED.

12b. DISTRIBUTION CODE

13. ABSTRACT *(Maximum 200 words)*
A study of the effects of mutual coupling and non-homogeneous data on the performance of adaptive algorithms (both covariance matrix based and least squared error) for Space Time Adaptive Processing (STAP). This effort addresses some of the issues in applying adaptive processing to real world, measured, data, by looking at the performance of two approaches: the JDL and D3 algorithms. Section 1.0 is an Introduction to the material in this report. Section 2.0 is a detailed analysis of the issue of mutual coupling and near field scattering. The section presents examples to illustrate the impact of mutual coupling on both D3 and statistical algorithms. Section 3.0 discusses the issues of non-homogeneous data, the use of a non-homogeneity detection and direct domain processing in non-homogeneous conditions.

14. SUBJECT TERMS
Space Time Adaptive Processing (STAP), Adaptive Array Processing (ASAP), Airborne Radar Signal Processing

15. NUMBER OF PAGES
76

16. PRICE CODE

17. SECURITY CLASSIFICATION OF REPORT	18. SECURITY CLASSIFICATION OF THIS PAGE	19. SECURITY CLASSIFICATION OF ABSTRACT	20. LIMITATION OF ABSTRACT
UNCLASSIFIED	UNCLASSIFIED	UNCLASSIFIED	UL

TABLE OF CONTENTS

List of Figures

List of Tables

1.0 Introduction

Airborne early warning radar systems operate in an environment that interferes with the reception of the target signal. The sources of interference could be deliberate jamming, non-hostile radio frequency interference, clutter and the noise inherent in any electrical system. The interference impacts on system performance by reducing the probability of target detection (P_d) and increasing the probability of false alarms (P_{fa}). These effects are further aggravated by inherent platform motion, multipath effects and a changing interference environment.

The traditional approach to interference suppression is to maximize the reception from the signal direction while minimizing the sidelobes in all other directions, i.e. the mainbeam gain is maximized while keeping the receiving antenna sidelobes below a prescribed level. This approach is useful only in relatively weak and static interference scenarios. In severe and dynamic interference scenarios, the traditional non-adaptive approach is inadequate and adaptive array techniques are required. The decisive advantage of an adaptive array is the ability to electronically steer the antenna mainlobe to any desired direction, while automatically placing deep pattern nulls in the specific direction of interference sources. This null placement is achieved automatically, without extensive *a priori* information about the interference scenario. Any required information is estimated in real time, using data received at the array.

Consider a phased array antenna with N spatial channels, possibly subarrays of a larger array. A series of M pulses is transmitted using this array. The M pulses form a Coherent Processing Interval (CPI). For each pulse, the return signal is sampled at a high rate, with each sample corresponding to a range cell. The number of samples per pulse determines the number of range cells. The received data can be visualized as a data cube with the spatial channels, pulses and range cells forming the three axes. The role of adaptive processing is to determine the location and speed of any targets that are in the data cube. The approach is to choose a particular range cell (the primary range cell) and determine the presence or absence of a target within that range cell. Spatially, the transmit direction sets the look angle, while the look Doppler varies over the entire Doppler spectrum. The adaptive process is repeated for each look Doppler after which the next range cell becomes the primary cell and the entire process is repeated.

Classical space-time adaptive processing (STAP) algorithms are based on the estimated covariance matrix of the interference [1]. The most straightforward STAP algorithm uses the NM dimensional covariance matrix of the interference to minimize the mean squared error with respect to the desired signal [2]. The algorithm obtains NM adaptive weights, resulting in a weighted combination of the NM data samples in the primary range cell. If the true covariance matrix of the interference is known, this traditional adaptive algorithm maximizes the output signal to noise ratio (SINR). In practice, the interference statistics are unknown and this matrix is estimated using secondary data obtained from range cells close to the primary range cell. An accurate estimate requires about $2NM$ to $3NM$ independent, identically distributed (i.i.d.) secondary data samples [3]. Typically, these samples are chosen from secondary data placed symmetrically about the range cell of interest.

The problem with this classical algorithm is that obtaining such a large number of i.i.d. samples is difficult, if not impossible. For example, urban areas and land-sea interfaces present the problem of large variations in terrain over relatively short distances. The resulting clutter returns show correspondingly large variations in statistics over short distances. In practice, it is impossible to accurately estimate the $NM \times NM$ interference covariance matrix. Another important concern with statistical approaches in general is the required computation load. Secondary data from cells in vicinity of the primary range cell must be stored and processed before the adaptive procedure can be applied. The covariance matrix must be updated regularly to reflect the changing interference conditions. Determining the NM adaptive weights requires the solution of NM dimensional matrix equation. As mentioned earlier, this process must be repeated for each look Doppler and each range cell. The entire process therefore involves a massive amount of computation that is supposed to be done in real time. This computation load is in itself prohibitively expensive.

Recently, to overcome some of these problems with classical statistical methods, some options have been investigated. Much of this work has focused on reducing the number of adaptive unknowns, equivalently the degrees of freedom (DOF), associated with the adaptive process. Reducing the number of adaptive unknowns (the size of the estimated covariance matrix) reduces the required secondary data [4]. Furthermore, estimating a smaller covariance matrix leads to a lower computation load. In particular, Wang and Cai introduce the Joint Domain Localized (JDL) processing algorithm, a post-Doppler, beamspace method [5]. The JDL algorithm uses very few DOF while retaining maximal gain against thermal noise.

There is one other important drawback with traditional statistical adaptive algorithms. The inherent assumption in estimating the covariance matrix is that the statistics of the secondary data is the same as the statistics of the interference in the primary range cell, i.e. the data cube is *homogeneous*. Statistical algorithms suffer from significant loss in performance when this assumption is violated. In practice, nonhomogeneous data is ubiquitous, with both natural and man made causes. Changes in terrain over short distances imply a corresponding change in the clutter characteristics with range. This problem is especially severe in airborne surveillance over land-sea interfaces and urban terrain. Man made non-homogeneities include vehicular ground traffic, corner reflectors, dense target environments, and active counter measures such as blinking jammers. In all these cases, the statistics of the interference fluctuates rapidly with distance and the secondary data required to obtain a good estimate of the covariance matrix is not available.

In response to the problem of non-homogeneous data, another major topic of research has been non-statistical methods that do not require a covariance matrix at all [6]. These methods use data from the range cell of interest only. Hence, these techniques bypass the problems of covariance matrix estimation associated with statistical approaches. Using the fact that an incident field presents a linear phase front at the receiver array, the signal component is cancelled. The resulting data has purely interference terms. Minimizing the total output power of these interference terms, while maintaining the antenna gain, leads to a least squared error solution. In [7], the algorithm of Sarkar and Sangruji [6] has been extended to account for beam mismatch. The least squares methods, also known as direct data domain (D^3) methods, show some promise to be significantly better than statistical approaches in dealing with non-stationary, non-homogeneous clutter.

Adaptive algorithms were originally developed for proof-of-concept, based on several idealizations of the real world. The performance of proposed algorithms were illustrated using simulated data that conformed to the idealizations. This approach has been effective in demonstrating the potential of STAP. However, in applying STAP algorithms to measured data, ignoring the effects of invalid idealizations leads to severe degradation of STAP performance. This effort addresses some of the issues in applying adaptive processing to real world, measured, data, by looking at the performance of the two approaches mentioned above: the JDL and D^3 algorithms. In particular, the two main issues addressed are:

- *Mutual Coupling*: Adaptive processing algorithms were formulated assuming the receiving antenna is a linear array of isotropic, point sensors. Such sensors spatially sample the field incident on the array without any re-radiation and there is no interaction or mutual coupling between the elements. However, such an array of ideal elements may be desirable, but is not achievable in practice. The elements must have some physical size. The elements spatially sample the incident fields *and* reradiate the fields. The reradiated fields interact with the other elements, resulting in mutual coupling between the elements of the array.
- *Nonhomogeneous Data*: As mentioned earlier, traditional adaptive processing algorithms are dependent on the assumption that the secondary data is homogeneous. Non-homogeneous data impacts significantly on the performance even low DOF algorithm such as JDL.

Section 2.0 is a detailed analysis of the issue of mutual coupling and near field scattering. The section presents examples to illustrate the impact of mutual coupling on both D^3 and statistical algorithms. In particular, this section presents the use of numerical electromagnetics, specifically the Method of Moments (MOM) to evaluate and compensate for the mutual coupling. Under the current effort, the impact of mutual coupling the JDL algorithm is presented. The formulation presented allows for the use of measurements to achieve compensation for mutual coupling without a detailed numerical analysis. Section 3.0 discusses the issues of non-homogeneous data, the use of a non-homogeneity detection and direct data domain processing in non-homogeneous conditions.

In this report, italicized letters denote scalars and integers, such as x and N, and lower case bold italic characters denote column vectors, e.g. $\mathbf{x}$. Upper case bold italic characters such as $\mathbf{R}$ denote matrices, while subscripts to bold characters represent the entries in the vector or matrix, such as $\mathbf{R}_{nm}$. The superscript ^{T} denotes the transpose and the superscript ^{H} denotes the conjugate transpose (Hermitian) of a vector or matrix.

2.0 Mutual Coupling and Near Field Scattering

Adaptive processing algorithms were originally developed assuming the receiving antenna to be a linear array of isotropic point sensors. In such a case, the sensors spatially sample the field incident on the array without any re-radiation. However, such an array of ideal elements may be desirable, but is not achievable in practice. The elements of the array must physically be some kind of antenna. They may be as simple as a wire dipole or more complicated such as a Yagi-Uda element. In either case, the elements not only spatially sample the incident fields, but also re-radiate the fields i.e. the antenna is a receiver *and* a scatterer. The re-radiated fields interact with the other sensors resulting in mutual coupling between the elements of the array.

Another assumption of the adaptive algorithms is that the array operates in a physical environment where nothing impedes the reception of the signals and interference. However, this assumption may not be satisfied in practice. The array is often in the presence of scatterers, which changes the environment in which the incident fields are received. For example, the fuselage of the aircraft, in airborne radar, changes the physical environment in which the incident fields are received. The effects of these near field scatterers are similar to the effects of mutual coupling between the elements of the array. This is because the scatterers, much like the array elements themselves, effect the signal reception by re-radiating the incident fields.

Gupta and Ksienski demonstrated the effects of mutual coupling on traditional statistical methods [8]. They base their analysis on a simple wire-dipole model for the array elements. They demonstrate that, even for large inter-element spacing, the mutual coupling causes significant degradation in the performance of the array. Since then, it has been shown that mutual coupling severely impacts on the performance of reduced rank algorithms such as JDL and non-statistical algorithms [9, 10]. In the case of the JDL algorithm, mutual coupling makes the Fourier transformation to angle space invalid [9]. In the case of direct data domain methods, the mutual coupling completely destroys the linear phase front that has been assumed for the incident fields [10]. Near field scatterers present similar problems. By re-radiating these fields, they destroy the linear phase front associated with the incident fields.

Mutual coupling between the elements of the antenna array and due to the near field scatterers is caused by the re-radiation of the incident field. This is a purely electromagnetic phenomenon. Therefore, to properly understand how the mutual coupling affects the adaptive algorithm, we need to properly understand the electromagnetic nature of the antenna array. Furthermore, the electromagnetic analysis of the array must be incorporated into the adaptive algorithm.

2.1 Method of Moments Analysis

The work of Gupta and Ksienski [8] is based on a formula given by Schelkunoff and Friis [11] for the mutual coupling between half wavelength dipoles separated by half a wavelength. This formula is equivalent to using a single sinusoidal basis function per element in a MOM type numerical analysis, an approach that is well known to be inadequate [12].

Using this formulation, Gupta and Ksienski develop a simple matrix equation to relate the open circuit voltages (voltages at the ports of the array if all ports were open circuited) with the given measured voltages. They suggest that the open circuit voltages are free of the effects of mutual coupling. However, this is not accurate. The open circuit voltages are the voltages in the presence of the other, open circuited, elements. The open circuited elements still re-radiate the incident fields and still contribute to the mutual coupling. Using open circuited voltages implies that the mutual coupling has been reduced, but not eliminated. This formulation is therefore valid only in low interference scenarios and cannot be used in the presence of near field scatterers. Several researchers have used this formulation for an initial analysis of the mutual coupling problem [13-15].

We present here a thorough MOM analysis of the mutual coupling problem based on the work of Adve and Sarkar [10]. The problem of signal recovery by a linear array of equispaced, thin, half wavelength dipoles is analyzed. For an accurate MOM analysis, multiple basis functions (unknowns) per element are used. Using a Galerkin formulation, the entries of the MOM impedance matrix measure the interaction between the basis functions, i.e. they quantize the mutual coupling.

Section 2.1.1 briefly presents the proposed MOM analysis. The antenna is modeled as a linear array of thin, identical, centrally point loaded dipoles. The MOM is then used to analyze the behavior of the array in the presence of an arbitrary incident field. This analysis leads to the MOM impedance matrix. MOM analysis of wire dipoles is well known [16]. However, the formulation is presented here to obtain the exact relationship between the incident fields with the measured voltages. This formulation will be crucial to the elimination of mutual coupling.

Section 2.1.2 presents the effects of mutual coupling on the performance of the D^3 algorithm of [6]. Section 2.1.3 presents a technique to compensate for the effects of mutual coupling. The proposed technique is tested on the example of Section 2.1.2. The technique is also compared to the compensation for mutual coupling using open circuit voltages as suggested by [8].

2.1.1 Method of Moments Analysis of Wire Dipoles

In an adaptive receiving system, an antenna array receives a signal corrupted by thermal noise and possibly external interference such as clutter and jammers. From an electromagnetics point of view, this can be treated as multiple incident fields impinging on the antenna. To understand the behavior of the antenna, we must therefore analyze its response to an arbitrary incident field.

The receiving antenna is assumed to be a linear array of N elements. The elements are parallel, thin, equispaced dipoles. Each element of the array is identically point loaded at the center. The dipoles are z-directed, of length L and radius a, and are placed along the x-axis, separated by distance Δx. The array lies in the X-Z plane.

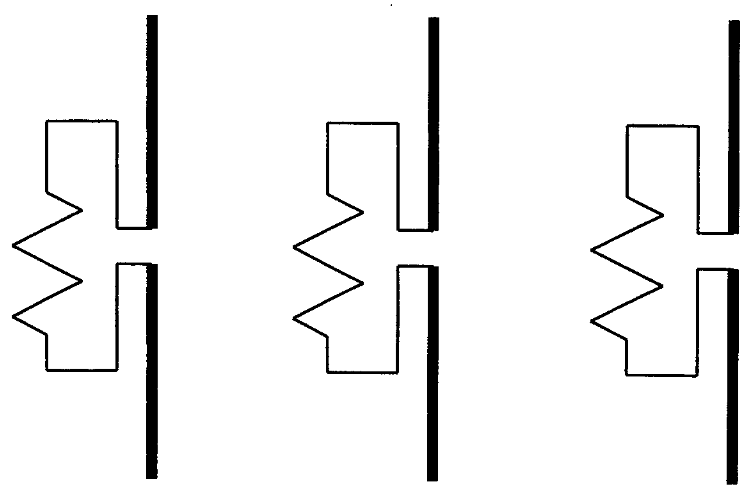

Figure 3: A linear array of wire dipoles

We begin by analyzing the response of the antenna array to a incident field $\mathbf{E}^{inc}$. Since the array is composed of thin wires the following simplifying assumptions are valid [17]:

- the current flows only in the direction of the wire axes (here the z direction.)
- the current and charge densities on the wire are approximated by filaments of current and charge on the wire axes (that lie in the $y=0$ plane)
- surface boundary conditions can be applied to the relevant axial component on the wire axes.

Based on these assumptions, the integral equation that relates the incident field to the current on the wires and describes the behavior of the array is

$$E_z^{inc}(z)=-\mu_0 \int_{axes} I(z')\frac{e^{-jkR}}{4\pi R}dz'+\frac{1}{\varepsilon_0}\frac{\partial}{\partial z}\int_{axes}\frac{\partial I(z')}{\partial z'}\frac{e^{-jkR}}{4\pi R}dz'. \tag{1}$$

We solve this equation using the Method of Moments to obtain the MOM impedance matrix. The basis functions used are piecewise sinusoids as described in [16] and shown in Figure 4. P (chosen odd) basis functions are used per element. Using these basis functions and a Galerkin formulation, Eqn. (1) is reduced to the matrix equation

$$[\mathbf{V}]=[\mathbf{Z}][\mathbf{I}] \Rightarrow [\mathbf{I}]=[\mathbf{Y}][\mathbf{V}], \tag{2}$$

where $[\mathbf{I}]$ is the MOM current vector with the coefficients of the expansion of the current in the sinusoidal basis. $[\mathbf{V}]$ is the MOM voltage vector representing the inner product of the weighting functions and the incident field. $[\mathbf{Z}]$ and $[\mathbf{Y}]$ are the MOM impedance and admittance matrices respectively. Both matrices are of order $NP \times NP$, where NP is the total number of unknowns used in the MOM formulation.

Assuming that the incident field is linearly polarized and arrives from direction (θ, ϕ), it can be written in the functional form

$$E_z^{\text{inc}} = E_0 e^{-j\mathbf{k}\cdot\mathbf{r}}, \tag{3}$$

where $\mathbf{k} = k[\hat{\mathbf{a}}_x \cos\phi \sin\theta + \hat{\mathbf{a}}_y \sin\phi \sin\theta + \hat{\mathbf{a}}_z \cos\theta]$ is the wave vector associated with the incident direction. Therefore, the i^{th} entry in the MOM voltage vector [**V**], corresponding to the q^{th} basis function on the m^{th} antenna, is given by the analytic form

$$V_i = \frac{E_0 e^{-jk(m-1)\Delta x \cos\phi \sin\theta}}{2} e^{-jkz_{q,m}\cos\theta} k \sin(k\Delta z) \sin^2\theta [\cos(k\Delta z \cos\theta) - \cos(k\Delta z)], \tag{4}$$

where $i = (m\text{-}1)P + q$ and Δz is the half the length of a single basis function.

The $(i,l)^{\text{th}}$ entry in the [**Z**] matrix is the inner product of the i^{th} basis function ($f_{q,m}$) with the z-component of the electric field due to a sinusoidal current source corresponding to the l^{th} basis function

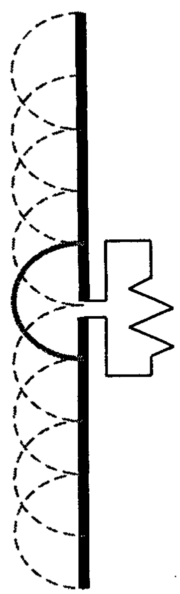

Figure 4: Piecewise sinusoidal basis functions for MOM analysis

($f_{p,n}$, $l=(p\text{-}1)P+n$). Therefore, the entries of the [**Z**] matrix are a measure of the interaction between different sections of the antenna array, that is, they are a measure of the mutual coupling between sections of the array. An analytic expression for the entries of the MOM impedance matrix is derived in [16].

Because of the choice of a piecewise sinusoid basis and the choice of an odd number of basis functions per antenna element, only one basis function is non-zero at the port. This is illustrated in Figure 4 where the basis function marked in bold is the only one contributing to the current at the port. Therefore, the measured voltage at the port of the n^{th} antenna is given by

$$V_{meas\_m} = Z_L I_{\frac{P+1}{2}}, \tag{5}$$

i.e. the measured voltage at a port of the array is directly proportional to the coefficient of the basis function corresponding to the that port.

The next section illustrates the effects of mutual coupling by comparing the ideal case of no mutual coupling between antenna elements with the case where mutual coupling is taken into account, but not compensated for. The effects are demonstrated on a direct data domain algorithm.

2.1.2 Effects of Mutual Coupling

In [6], Sarkar and Sangruji present a direct data domain technique to adaptively recover a desired signal arriving from a given look direction while simultaneously rejecting all other interference. The technique is based on the fact that, in the absence of mutual coupling, a far field source presents a linear phase front at the ports of a linear array. In this section, we demonstrate that the mutual coupling undermines the ability of this algorithm to maintain the gain of the array in the direction of the signal while simultaneously rejecting the interference. To do so we compare the performance of the algorithm in the ideal case of mutual coupling with the case where mutual coupling is taken into account, but not compensated for. We begin by briefly describing the adaptive technique developed in [6].

2.1.2.1 Least Squared Error Adaptive Nulling

Consider an array of N uniformly spaced isotropic point sensors as shown in Figure 3. The array receives a signal from a known azimuthal direction ϕ_0 and some interference sources from unknown directions. In the absence of mutual coupling, each individual source presents a linear phase progression across the face of the array. Therefore, the voltage at the i^{th} element due to the incident fields is

$$V_i = Se^{jk(i-1)\Delta x \cos\phi_0} + \sum_{l=1}^{L} J_l e^{jk(i-1)\Delta x \cos\phi_l} + n_i, \tag{6}$$

where S is the complex strength of the signal component, J_l represents the L interfering components that arrive from directions ϕ_l and n_i is the additive noise component. Let $\beta = e^{jk\Delta x \cos\phi_0}$ represent the phase progression of the signal component from one element to the next. The term $V_i - \beta^{-1} V_{i+1}$ therefore has no signal component. Consider the $K \times K$ matrix equation given by

$$\begin{bmatrix} 1 & \beta & \cdots & \beta^{K-1} \\ V_1 - \beta^{-1}V_2 & V_2 - \beta^{-1}V_3 & \cdots & V_K - \beta^{-1}V_{K+1} \\ \vdots & \vdots & \cdots & \vdots \\ V_{K-1} - \beta^{-1}V_K & V_K - \beta^{-1}V_{K+1} & \cdots & V_{N-1} - \beta^{-1}V_N \end{bmatrix} \begin{bmatrix} w_1 \\ w_2 \\ \vdots \\ w_K \end{bmatrix} = \begin{bmatrix} 1 \\ 0 \\ \vdots \\ 0 \end{bmatrix}, \tag{7}$$

where $K = (N+1)/2$.

The last (K-1) rows of the matrix contain only interference and noise terms. Setting the product of these terms with the weights to zero, nulls the interference in a least squared sense. The equation represented by the first row constrains the array gain in the direction of the signal. It can be shown that if $L+1 < K$, the signal can be recovered and

$$S = \sum_{k=1}^{K} w_i V_i, \tag{8}$$

2.1.2.2 Numerical Examples

An example demonstrates the effect of mutual coupling between the elements of the array on the algorithm described in Section 2.1.2.1. In each example an array receives a signal corrupted by three jammers. To focus only on the effects of mutual coupling these examples neglect thermal noise.

For each example two scenarios are compared. In the first scenario the ideal case of no mutual coupling is assumed and the voltages at the array ports are given by Eqn.(6). These voltages are then passed to the signal recovery subroutine to find the weights using Eqn. (7) and the signal is estimated using Eqn. (8).

In the second scenario the mutual coupling is taken into account. The antenna is analyzed using the Method of Moments. The intensities of the signal and interference and their directions of arrival, in conjunction with Eqn. (4), are used to calculate the Method of Moments voltage vector. Equation (5) is used to find the voltages that are measured across the load at the individual ports. These measured voltages are input to the signal recovery subroutine. The signal intensity is then recovered using Eqn. (8). No attempt is made to compensate for mutual coupling.

The details of the chosen array are presented in Table 1.

Table 1: Details of example array

Number of elements in the array	7
Length of z-directed wires	$\lambda/2$
Radius of z-directed wires	$\lambda/200$
Spacing between wires	$\lambda/2$
Loading at the center	50 Ω

Table 2 lists the base signal and jammer values for the examples presented. All signals and jammers arrive from the elevation $\theta=90^o$.

Table 2: Base signal and jammer values

	Magnitude	Phase	DOA
Signal	1.0 V/m	0.0	45^o
Jammer #1	1.5 V/m	0.0	75^o
Jammer #2	2.0 V/m	0.0	60^o
Jammer #3	1.0 V/m	0.0	30^o

The receiving algorithm attempts to maintain the gain of the array in the direction of $\phi_0 = 45^o$ while automatically placing nulls at in the interference directions. In all simulations the jammer intensities, the directions of arrival of the jammers and the signal intensity are used only to find the voltages input to the receiving algorithm. The receiving algorithm itself uses only the direction of arrival of the signal, i.e. only the look direction is assumed known.

2.1.2.3 Numerical Example 1

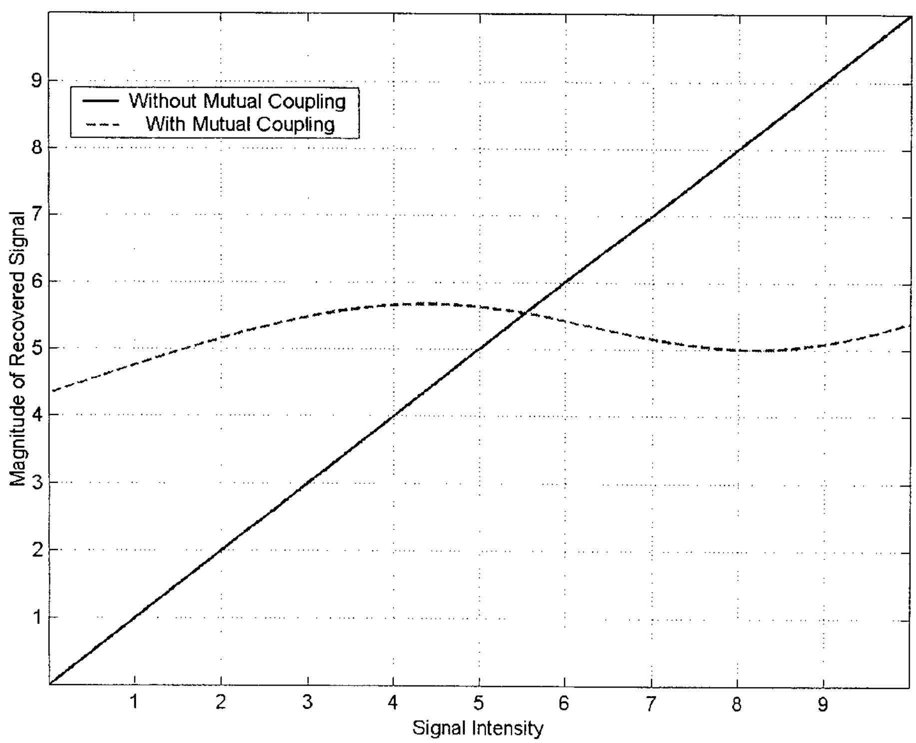

Figure 5: Signal recovery in the presence and absence of mutual coupling.

In this example, the interference is kept constant as shown in Table 2. The signal value is varied between 0 V/m and 10 V/m. For each value of signal intensity the voltages in the absence of mutual coupling are found. These values are passed to the receiving algorithm and the signal is reconstructed. If the jammers have been nulled correctly, and the signal recovered properly, it is expected that the reconstructed signal will have a linear relationship with respect to the intensity of the incident signal.

Figure 5 plots the results of using the algorithm presented in Section 2.1.2.1 to recover the signal in the presence of jammers, but in the absence of mutual coupling. As can be seen, this magnitude displays the expected linear relationship.

In the second scenario, for each value of the signal intensity, mutual coupling is taken into account and the measured voltages are obtained using the MOM. Figure 5 also presents the results of using data influenced by mutual coupling. As can be seen, in the presence of mutual coupling, the reconstruction is completely inaccurate. As the signal value is increased, the reconstructed signal presents a non-linear behavior.

2.1.2.4 Numerical Example 2

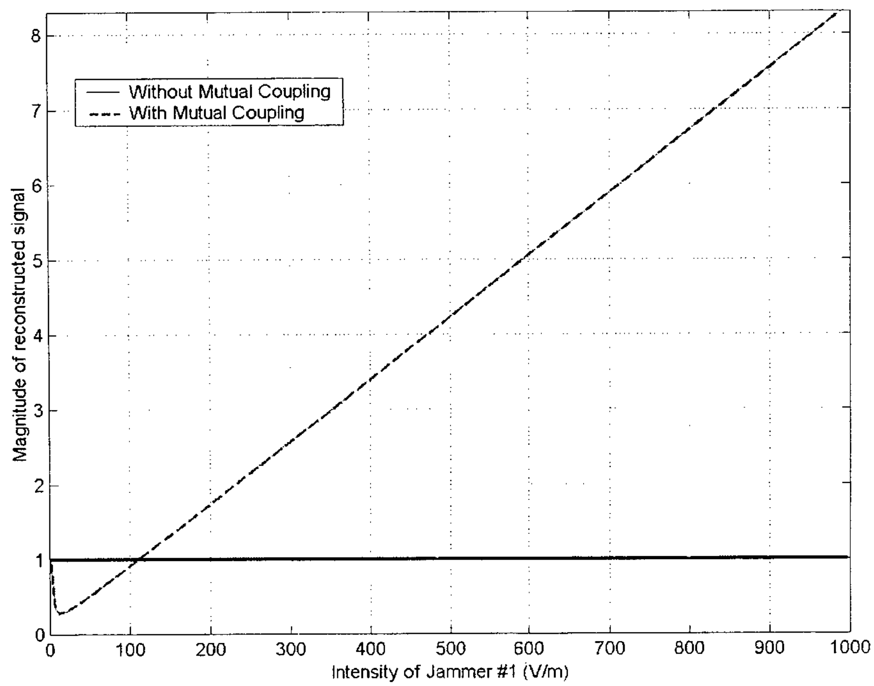

Figure 6: Reconstructed signal as function of jammer intensity, without and with mutual coupling

In the second example, the signal is kept constant at 1.0 *V/m* as given in Table 1. The intensity of first jammer, arriving from $\phi = 75^{o}$, is varied from 1.0 *V/m* (0 dB with respect to the signal) to 1000.0 *V/m* (60 dB) in steps of 5.0 *V/m*. The example compares the performance of the adaptive algorithm in the absence of mutual coupling (the ideal case) with the performance in the presence of mutual coupling (the realistic case). No compensation for mutual coupling is performed. If the jammers are properly nulled, we expect the reconstructed signal to have no residual jammer component. Therefore, as the jammer strength is increased, we expect the reconstructed signal to remain constant.

Figure 6 presents the results of using the receiving algorithm when mutual coupling is absent and when it is present. The figure plots the magnitude of the reconstructed signal as a function of jammer intensity. In the case of mutual coupling absent (the solid line), the reconstructed signal is indistinguishable from the expected value of 1.0 *V/m*. This figure demonstrates that, in the absence of mutual coupling, the receiving algorithm is highly accurate and can null a strong jammer. The dashed line in Figure 6 shows the results of using the measured voltages that are affected by mutual coupling. The magnitude of the reconstructed signal varies approximately linearly with respect to the intensity of the jammer. This is because the strong jamming is not nulled and the residual jammer component completely overwhelms the signal.

Figure 5 and Figure 6 illustrates the problem with applying a purely signal processing algorithm without paying attention to the electromagnetic issues. In the realistic case of mutual coupling present, even an effective signal processing algorithm fails totally. The reason the signal cannot be recovered when mutual coupling is taken into account can be visually understood by comparing the adapted beam patterns in the ideal case of no mutual coupling with the case where mutual coupling is present. In Figure 7, we see the beam patterns in two scenarios. The pattern clearly displays the three deep nulls at the directions of the interference. The high sidelobes are in the region where there is no interference. Because of the deep nulls, the strong interference can be completely nulled and the signal recovered correctly.

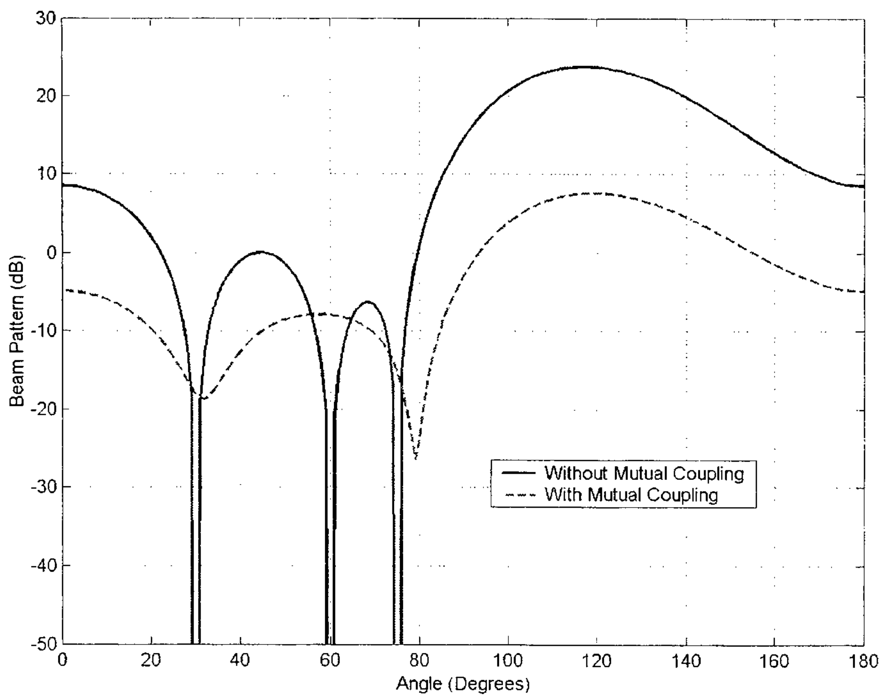

Figure 7: Adapted beam patterns in the absence and presence of mutual coupling

The dashed line in Figure 7 shows the beam pattern when the mutual coupling is taken into account. As is clear the gain of the antenna in the signal direction is considerably reduced, the pattern nulls are shallow and are displaced from the desired locations. The shallow nulls result in the inadequate nulling of the interference, hence the signal cannot be recovered.

The examples presented here illustrate the importance of the problem at hand. When mutual coupling is taken into account not only is the main beam of the adaptive array is pointed in the wrong direction, but also the ability to form deep nulls in the directions of the interference is considerably rediuced. In summary, the mutual coupling between the elements undermines the ability of the algorithm to suppress interference.

In summary, the least squared nulling (or D^3) algorithm of Section 2.1.2.1 is a promising alternative to classical statistical algorithms. However, using the voltages measured at the ports of the array yields incorrect results and the mutual coupling between the elements undermines the ability of the algorithm to suppress interference. The next section presents a technique to compensate for the effects of mutual coupling for linear dipole arrays. This technique is more effective than the compensation technique of [8].

2.1.3 Compensation for Mutual Coupling

Most adaptive algorithms assume that each element in the array is independent of the other elements in the array. The mutual coupling arises due to the re-radiation of the incident fields from the elements themselves. To eliminate the effects of mutual coupling, we begin by realizing that the MOM voltages of Eqn. (4) relate directly to the incident fields and so are not affected by mutual coupling. The approach here therefore will be to recreate some part of the MOM voltage vector from the given measured voltages.

The Method of Moments analysis results in a matrix equation that relates the coefficients of the current expansion to the MOM voltages through the admittance matrix. Since the MOM impedance and admittance matrices are independent of the incident fields, they can be evaluated *a priori*.

The measured voltages at the ports of the antenna are related to the current coefficients by Eqn. (5). Using this equation and Eqn. (2), the N dimensional vector of measured voltages, corresponding to the N elements in the array, can be written as

$$[\mathbf{V}]_{meas} = [\mathbf{Z}_L][\mathbf{Y}_{port}][\mathbf{V}], \tag{9}$$

where $[\mathbf{Z}_L]$ is the $N \times N$ diagonal matrix with the load impedances at its entries, $[\mathbf{Y}_{port}]$ is the matrix with the rows of the MOM impedance matrix $[\mathbf{Y}]$ that correspond to the ports of the array. $[\mathbf{V}]$, the MOM voltage vector is of order NP, i.e. the number of unknowns in the MOM analysis. $[\mathbf{Y}_{port}]$ is a rectangular matrix of order $N \times NP$.

Since $[\mathbf{Y}_{port}]$ is a matrix with more columns than rows ($P > 1$), Eqn. (9) represents an underdetermined system of equations. Our goal is to estimate some part of $[\mathbf{V}]$ given $[\mathbf{V}]_{meas}$. Therefore, we need a method to collapse the $N \times NP$ matrix $[Y_{port}]$ to a $N \times N$ matrix.

The approach is best understood when illustrated with an example. Consider the case of a two element array (N=2) and three unknowns per element (P=3). Then basis function #2 corresponds to the port on the first element and basis function #5 to the port on the second element. In this case, Eqn. (9) can be written as

$$\begin{bmatrix} \mathbf{V}_{meas\,1} \\ \mathbf{V}_{meas\,2} \end{bmatrix} = \begin{bmatrix} \mathbf{Z}_L & 0 \\ 0 & \mathbf{Z}_L \end{bmatrix} \begin{bmatrix} \mathbf{Y}_{21} & \mathbf{Y}_{22} & \mathbf{Y}_{23} & \mathbf{Y}_{24} & \mathbf{Y}_{25} & \mathbf{Y}_{26} \\ \mathbf{Y}_{51} & \mathbf{Y}_{52} & \mathbf{Y}_{53} & \mathbf{Y}_{54} & \mathbf{Y}_{55} & \mathbf{Y}_{56} \end{bmatrix} \begin{bmatrix} \mathbf{V}_1 \\ \mathbf{V}_2 \\ \mathbf{V}_3 \\ \mathbf{V}_4 \\ \mathbf{V}_5 \\ \mathbf{V}_6 \end{bmatrix}, \tag{10}$$

If the jammers and signal are all incident from approximately the same elevation θ, then the entries of the length-NP vector are not all independent of each other. From Eqn.(4), if element i and i+1 belong to the same element,

$$\mathbf{V}_i = e^{-jk\Delta z\cos(\theta)}\mathbf{V}_{i+1}, \tag{11}$$

Letting $\alpha = e^{jk\Delta z\cos(\theta)}$, we have

$$\begin{aligned} \mathbf{V}_1 &= e^{-jk\Delta z\cos(\theta)}\mathbf{V}_2 = \alpha^{-1}\mathbf{V}_2, \\ \mathbf{V}_3 &= e^{jk\Delta z\cos(\theta)}\mathbf{V}_2 \ = \alpha\mathbf{V}_2, \\ \mathbf{V}_4 &= e^{-jk\Delta z\cos(\theta)}\mathbf{V}_5 = \alpha^{-1}\mathbf{V}_5, \\ \mathbf{V}_6 &= e^{jk\Delta z\cos(\theta)}\mathbf{V}_5 \ = \alpha\mathbf{V}_5, \end{aligned} \tag{12}$$

and

$$\begin{bmatrix} \mathbf{V}_{meas\,1} \\ \mathbf{V}_{meas\,2} \end{bmatrix} = \begin{bmatrix} \mathbf{Z}_L & 0 \\ 0 & \mathbf{Z}_L \end{bmatrix} \begin{bmatrix} \alpha^{-1}\mathbf{Y}_{21} + \mathbf{Y}_{22} + \alpha\mathbf{Y}_{23} & \alpha^{-1}\mathbf{Y}_{24} + \mathbf{Y}_{25} + \alpha\mathbf{Y}_{26} \\ \alpha^{-1}\mathbf{Y}_{51} + \mathbf{Y}_{52} + \alpha\mathbf{Y}_{53} & \alpha^{-1}\mathbf{Y}_{51} + \mathbf{Y}_{52} + \alpha\mathbf{Y}_{53} \end{bmatrix} \begin{bmatrix} \mathbf{V}_2 \\ \mathbf{V}_5 \end{bmatrix}. \tag{13}$$

This equation is a square matrix equation that may be solved for the entries in the MOM voltage vector corresponding to the ports.

Equation (13) is a relation between the measured voltages and the Method of Moments voltages that correspond to the ports of the array. In a practical application, the measured voltages are the given quantities and are affected by mutual coupling. The MOM voltages on the right hand side of Eqn. (13) are the voltages that are directly related to the incident fields and so are free from the effects of mutual coupling. Both vectors are of order N, the number of ports.

Therefore, this equation can be solved for the MOM voltages corresponding to the ports of the antenna. Furthermore, if the elevation angle of interest (θ) is fixed, the matrix can be evaluated *a priori*. Hence, the computational cost of eliminating the mutual coupling is the limited to the solution of small matrix equation.

The open circuited voltages are the voltages measured at the ports of the array if the ports were open circuited. In [8] the authors assume that these voltages are free of the effects of mutual coupling. However the open circuit voltage at a particular element is the voltage measured in the presence of the other open circuited elements. The effect of mutual coupling, therefore, has been reduced but not eliminated. Mutual coupling has been eliminated only when there is nothing impeding the path of the incident fields. In effect not even the array itself.

The next four sections present examples to illustrate the efficacy of the formulation presented above. The first two examples are the same as in Sections 2.1.2.3 and 2.1.2.4. For these two examples the use of open circuit voltages as suggested by [8] is compared with the use of the voltages found from Eqn. (13).

2.1.3.1 Numerical Example 1

The seven element array defined in Table 1 receives a signal corrupted by three jammers. The base signal and jammer strengths are as given in Table 2. The magnitude of the incident signal is varied from 0 *V/m* to 10.0 *V/m* in steps of 0.05 *V/m* while maintaining jammer intensities constant as given in the table. For each value of the signal intensity the MOM voltage vector is evaluated to yield the measured voltages. The measured voltages and the signal DOA are treated as the known quantities.

Using the measured voltages and MOM admittance matrix, the open circuit voltages are obtained. These open circuit voltages are passed to the direct data domain algorithm described in Section 2.1.2.1 and an attempt is made to recover the signal. It is expected that the recovered signal varies linearly with the intensity of the incident signal. Figure 8(a) presents the results of using the open circuit voltages. The expected linear relationship is clearly seen, implying that the jammers have been nulled and the signal recovered correctly. The numerical value of the signal is correct within a calibration constant.

In the second scenario, the measured voltages are used to recover the vector of voltages without mutual coupling. Figure 8(b) shows the results of using these recovered voltages to recover the signal. Again, the expected linear relationship is clearly visible. This example has shown that open circuit voltages do provide some compensation for mutual coupling. The use of open circuit voltages provides for significantly better signal recovery than using the measured voltages directly. The technique to eliminate the effects of mutual coupling introduced in 2.1.3 also proves to compensate for mutual coupling. In this example, however, the interference was relatively weak. A more stringent test for both compensation techniques is to check their ability to suppress strong interference.

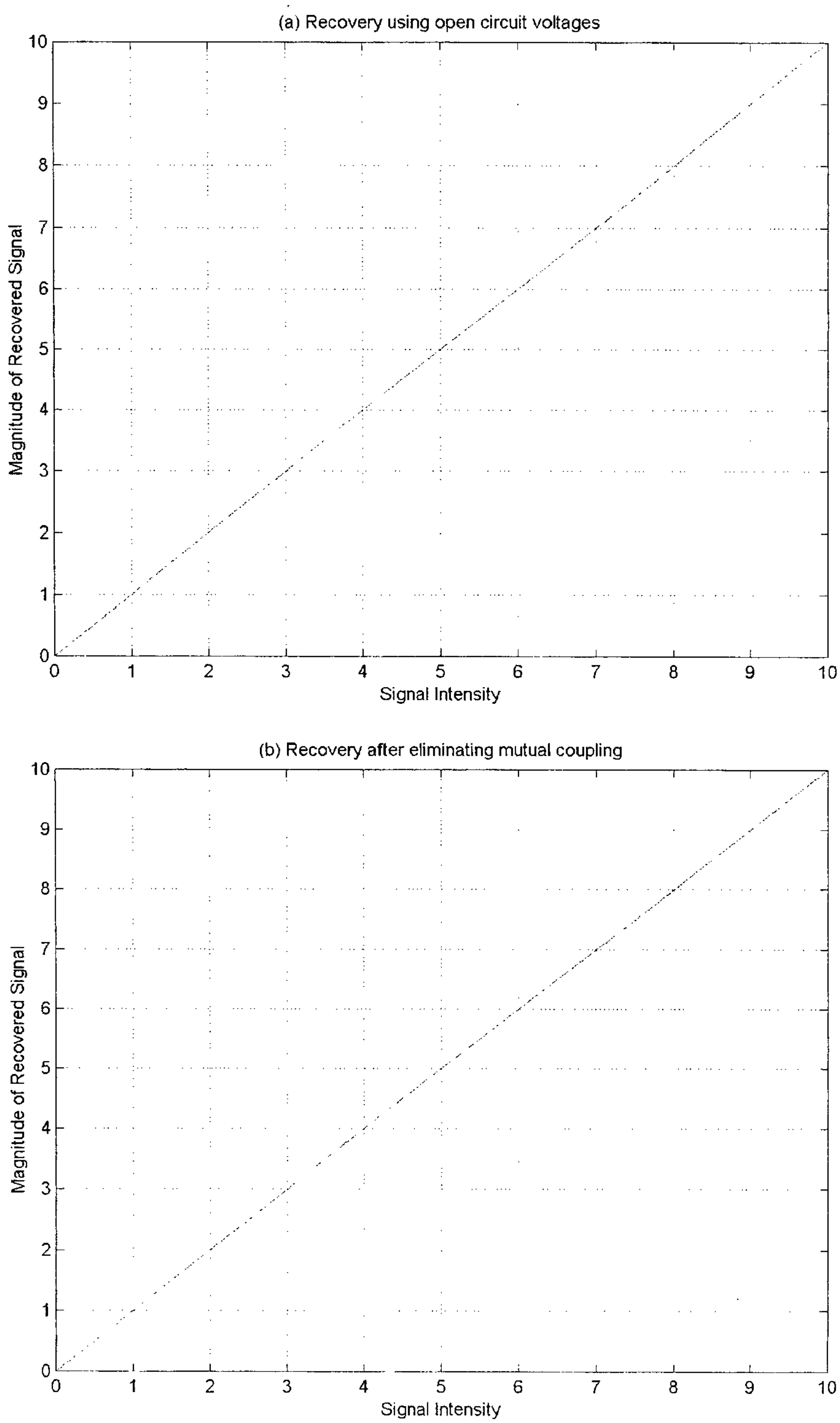

Figure 8: Signal recovery using open circuit voltages and after eliminating mutual coupling

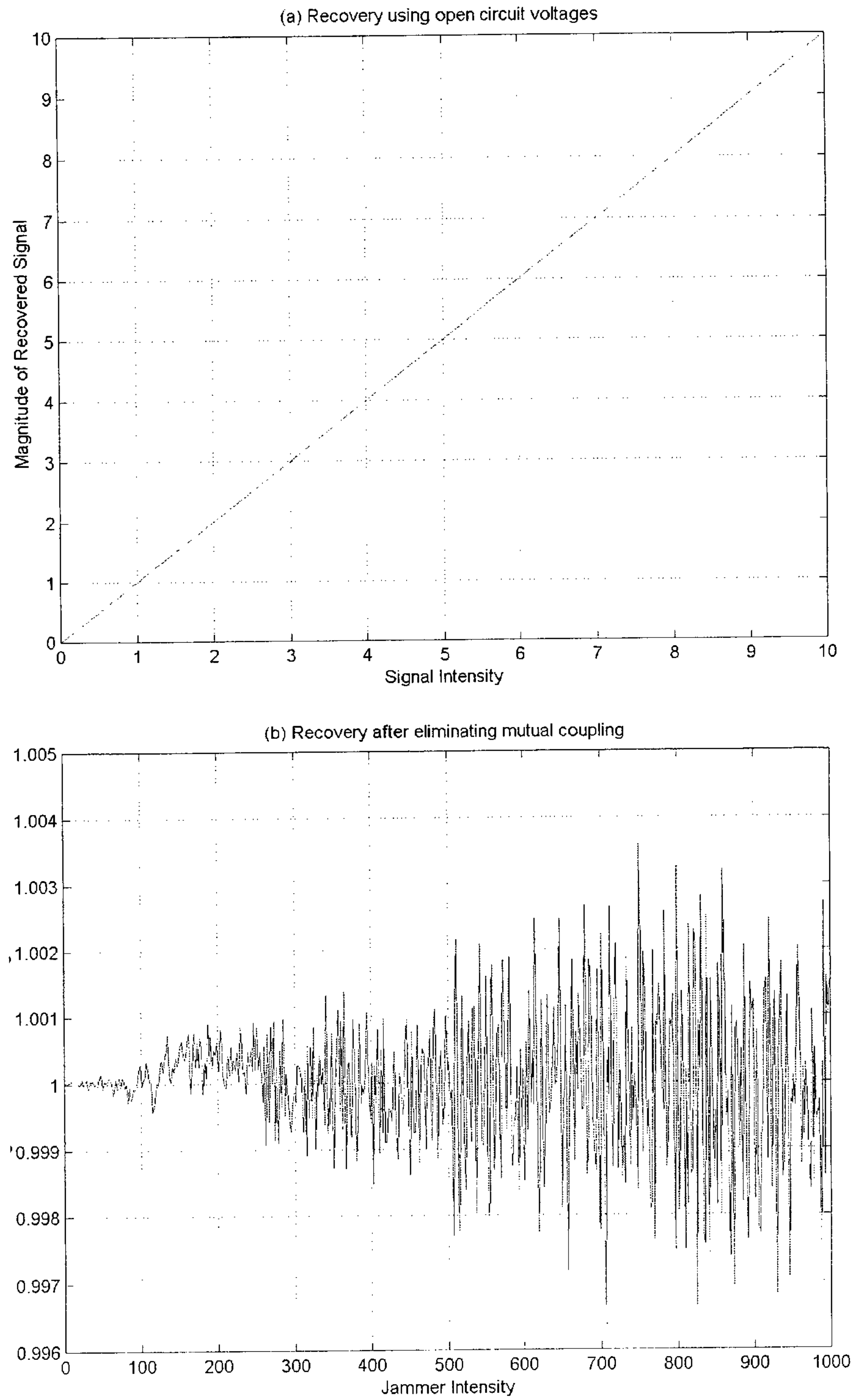

Figure 9: Signal recovery using open circuit voltages and after eliminating mutual coupling

2.1.3.2 Numerical Example 2

In the second example, the intensity of the incident signal is held constant at 1.0 *V/m*. The intensity of the first jammer is varied from 1.0 *V/m* to 1000 *V/m* (60 dB above the signal) in steps of 5 *V/m*. For each value of the jammer intensity, the MOM voltage vector is calculated and the measured voltages are calculated. In the first scenario the measured voltages are used to find the open circuit voltages. The open circuit voltages are passed to the direct data domain algorithm of Section 2.1.2.1. In the second scenario the voltages after eliminating mutual coupling, using Eqn. (13) as suggested here, are used to recover the signal. These voltages are used to recover the signal and null the jammers using the same algorithm. If the jammers are properly nulled, the reconstructed signal magnitude should remain constant as a function of jammer strength.

Figure 9(a) presents the results when the open circuit voltages are used to recover the signal. As can be seen the recovered signal shows a near linear relationship a function of jammer strength. This indicates that the jammer has not been adequately nulled and the residual jammer strength has overwhelmed the signal.

Figure 9(b) plots the results of compensating for the mutual coupling using the technique presented in this report. The magnitude of the reconstructed signal varies between 0:996 *V/m* and 1.004 *V/m*, i.e. the error in the signal recovery is very small. This figure shows that the strong jammer has been effectively nulled and the signal can be reconstructed.

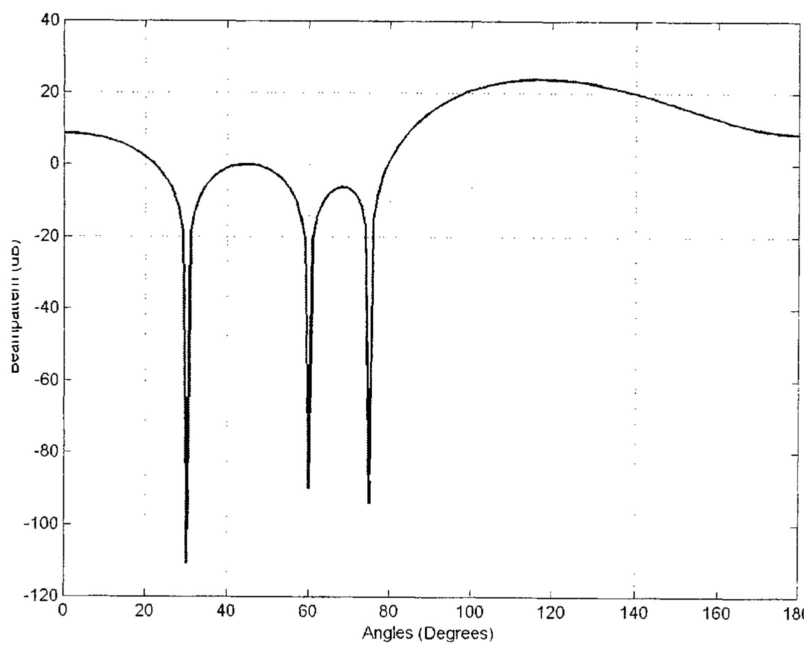

Figure 10: Beam pattern after eliminating mutual coupling

The beam pattern associated with compensating for the mutual coupling using the technique presented in this report is shown in Figure 10. The nulls are deep and placed in the correct directions. This demonstrates that the mutual coupling has been suppressed enough so as to null even a strong jammer.

2.1.3.3 Example 3: Effect of noise

The examples presented above illustrate the effects of mutual coupling and ignored the additive noise at each antenna element. This example presents the effect of thermal noise on the adaptive algorithm. The noise is additive and is modeled as a Gaussian random variable. The noise at any element is assumed independent of the noise at the other elements. Since the noise introduces a random component to the data, comparisons will be made using Monte Carlo simulations, in terms of averages over many random samples.

Table 3: Signal and Jammer Values. Example 3

	Magnitude (dB)	Phase	DOA
Signal	1.0	0.0	85^o
Jammer 1	2000.0	0.0	135^o
Jammer 2	1.0	0.0	60^o
Jammer 3	1.0	0.0	100^o

In this example, a thirteen element array of thin, half-wavelength long, wire dipoles receives a signal corrupted by three jammers as given in Table 3. The z-directed dipoles each have radius $\lambda/2200$ and are spaced half a wavelength apart. Each wire is centrally loaded with a 50Ω resistance.

Seven unknowns per wire are used in the Method of Moments analysis, leading to a total of 91 unknowns. The signal to noise ratio was set at 13dB. Note that jammer #1 is a strong jammer (66dB with respect to the signal). For each of the 13 channels, a complex Gaussian random variable is added to the measured voltages due to the signal and jammers. This set of voltages, affected by noise, is passed to the signal recovery routine described in Section 2.1.2.1. This procedure is repeated 500 times with different noise samples. These 500 samples are used to find the mean and variance. The output signal to interference plus noise ratio (SINR) in dB is defined as

$$SINR_{out} = 10\log_{10}\left[\frac{|S|^2}{bias^2 + \mathrm{var}}\right], \tag{14}$$

with bias defined as the difference between the true and mean signal values after 500 iterations.

Table 4: Performance of Direct Data Domain after compensating for mutual coupling

	Before compensating for mutual coupling	After compensating for mutual coupling
Signal to Noise Ratio	13 dB	13 dB
Number of samples	500	500
True Value	(1.0,0.0)	(1.0,0.0)
Mean Value	(0.93337,0.49295)	(1.00379,-0.00298)
Bias	(-0.06663,0.49295)	(0.00379,-0.00298)
Variance	0.01044	0.01038
Output SINR	6.35526	19.86559

Table 4 summarizes the results of this example. When the measured voltages are used directly to recover the signal, mainly due to the high bias in the estimate of the signal, the output SINR is only 6.35526dB. The high bias can be directly attributed to the inadequate nulling of the strong jammer. However, when the mutual coupling is eliminated using the technique presented in this report, the jammers are completely nulled yielding accurate estimates of the signal. The total interference power is suppressed to nearly 20dB below the signal.

The examples presented here demonstrate that the method proposed in this Section 2.1.3 is an effective compensation for the effects of mutual coupling. Using the Method of Moments with multiple basis functions per element allows us to reduce the mutual coupling to an extent where it is inconsequential.

This section has demonstrated that, for the development of practical direct data domain algorithms, the electromagnetic nature of the array must be taken into account. We have shown that the mutual coupling between the elements of the array causes adaptive algorithms to fail. This problem is associated with both covariance matrix approaches (stated earlier by [8]) and direct data domain approaches (investigated here).

To properly characterize the antenna, the Method of Moments is used. Previously published work in this area has used only one basis function per element. However, this is usually inadequate for an accurate antenna analysis. The use of multiple basis functions per element in a practical manner is a major advance over previously published methods. The mutual coupling is eliminated by recognizing that the MOM voltage vector is free from mutual coupling. By using a relationship between the entries of the MOM voltage vector, a square matrix equation is developed between the given measured voltages and the relevant entries of the MOM voltage vector. It is shown that this method works very well in the presence of strong interfering sources. Furthermore, it is shown that the proposed technique is superior to the earlier suggested method of using the open circuit voltages.

In summary, this section has investigated a topic that is very important to the development of practical adaptive algorithms. The proposed method is easy to implement and does not add an inordinate computational burden on the adaptive process.

2.2 Mutual Coupling and Statistical Algorithms

Classical statistical STAP algorithms estimate a covariance matrix of the interference using data from range cells close to the range cell of interest. The adaptive weights ($\mathbf{w}$) are then obtained using

$$\mathbf{R}\mathbf{w} = \mathbf{s} \Rightarrow \mathbf{w} = \mathbf{R}^{-1}\mathbf{s}, \tag{15}$$

where, $\mathbf{s}$ is the space-time steering vector that sets the look direction (the angle and Doppler at which a target is being searched). The steering vector is given by

$$\mathbf{s}(\phi, f_d) = \mathbf{b}(f_d) \otimes \mathbf{a}(\phi), \tag{16}$$

where $\mathbf{b}(f_d)$ is the temporal steering vector corresponding to normalized Doppler frequency f_d, $\mathbf{a}(\phi)$ is the spatial steering vector corresponding to the look angle ϕ and $\otimes$ denotes the Kronecker product of two matrices. The temporal steering vector is the M-element vector (note that M is the number of pulses in a CPI) given by

$$\mathbf{b}(\phi) = \left[1 \quad e^{j2\pi f_d} \quad e^{j2\times 2\pi f_d} \ldots e^{j(M-1)2\pi f_d}\right]^T. \tag{17}$$

The spatial steering vector is the response of the antenna array to an incident field that arrives from the angle of interest. In the ideal case of a linear array of isotropic point sensors, the steering vector for the N-element array is given by

$$\mathbf{a}(\phi) = \left[1 \quad e^{jkd\cos(\phi)} \quad e^{j2kd\cos(\phi)} \ldots e^{j(N-1)kd\cos(\phi)}\right]^T. \tag{18}$$

Note that the derivation of the D^3 algorithm in Section 2.1.2.1 for an ideal array assumes this form of the steering vector. There is an belief that by replacing the ideal steering vector of $\mathbf{a}(\phi)$ in Eqn. (16) with the a "true" steering vector mutual coupling does not impact on statistical algorithms. This "true" steering vector may be obtained using either measurements or numerical electromagnetics analyses such as the Method of Moments. However, this section will show that mutual coupling has other effects that must be accounted for in the formulation or implementation of space-time adaptive processing.

2.2.1 Impact on Structure of Covariance Matrix

In the case of an ideal array, the spatial interference covariance matrix is Toeplitz. In the space-time case, the space-time data vector can be arranged such that the covariance matrix is Toeplitz-Block-Toeplitz. In the ideal case, each element of the array is independent of the others and the correlation between elements is only a function of the distance between them. However, this is true only under the ideal case. In a real array, each element in the array sees a different environment. The correlation between two elements is a function of the distance between them and also the location of the elements in the array.

Table 5: Covariance matrices: without and with mutual coupling

Without Mutual Coupling							*With Mutual Coupling*						
0.92	0.59	0.59	0.41	0.37	0.22	0.23	0.80	0.76	0.57	0.44	0.28	0.23	0.01
0.59	0.85	0.58	0.66	0.43	0.42	0.23	0.96	0.96	0.75	0.54	0.35	0.29	0.10
0.59	0.58	0.86	0.60	0.59	0.41	0.38	0.57	0.75	0.82	0.66	0.45	0.40	0.20
0.41	0.66	0.60	1.00	0.63	0.64	0.34	0.44	0.54	0.66	0.86	0.68	0.59	0.39
0.37	0.43	0.59	0.63	0.88	0.62	0.56	0.28	0.35	0.45	0.68	0.83	0.77	0.50
0.22	0.42	0.41	0.64	0.62	0.90	0.60	0.23	0.29	0.40	0.59	0.77	1.00	0.71
0.23	0.23	0.38	0.34	0.56	0.60	0.88	0.01	0.10	0.20	0.39	0.50	0.71	0.73
Measure of "Non-Toeplitzity" = 0.1926							Measure of "Non-Toeplitzity" = 0.4827						

To illustrate this point, Table 5 presents the magnitude of each element of the covariance matrix for the case with and without mutual coupling. The array has seven elements spaced $\lambda/2$ apart. Each element is of length $\lambda/2$ and radius $\lambda/200$. The clutter is 25dB above the noise. 28 secondary data vectors are used to estimate the 7×7 covariance matrix. The covariance matrices are normalized to the maximum absolute value. The "Non-Toeplitzity" of the matrix is defined as mean squared summed error between the matrix and its Hermitian. Mutual coupling is analyzed using the MOM as described in Section 2.1.1.

As can be seen, the covariance matrix is approximately Toeplitz in the ideal case of no mutual coupling. In the case of mutual coupling the covariance matrix is significantly non-Toeplitz. Solving for the weights assuming a Toeplitz matrix leads to incorrect solutions.

While the above discussion relates to the implementation of a STAP algorithm in hardware, the following example presents a more important impact of mutual coupling on the performance of STAP algorithms. For an ideal array, the number of significant clutter eigenvalues is set by the number of pulses in a CPI, number of elements and speed of the platform. In general [4]

$$N_{eig} = N + \beta(M-1), \tag{19}$$

where, β is the number of half element spacings that the aircraft transverses in a single pulse interval. In this example, the seven-element array is used in conjunction with three pulses to form a CPI, i.e. $N = 7$ and $M = 3$ and the size of the covariance matrix is 21×21. The speed of the aircraft is set such at $\beta=1$, i.e. the number of significant eigenvalues is 9. We use 84 secondary data vectors to estimate the 21×21 covariance matrix. The eigenvalue spread for the case without and with mutual coupling is given in Fig.1.

As can be seen, the eigenvalue plot for the case without mutual coupling shows a sharp cutoff at the 9th eigenvalue. For the case with mutual coupling, the cut off is significantly smoother.

The figure shows that in the case of mutual coupling, the number of significant clutter eigenvalues is much larger than in the ideal case. This point is of particular importance in statistical algorithms that depend on separating a signal subspace and noise subspace. In STAP, examples of such algorithms are the principal components technique and the Cross Spectral Metric (CSM). **INCLUDE PC AND CSM REERENCES.** In the area of direction of arrival estimation algorithms, such as the popular MUSIC algorithm, also attempt to separate the signal and noise subspaces. The impact of the spread of eigenvalues will lead to significantly reduced detection performance for the STAP algorithms and poor resolution in direction of arrival algorithms.

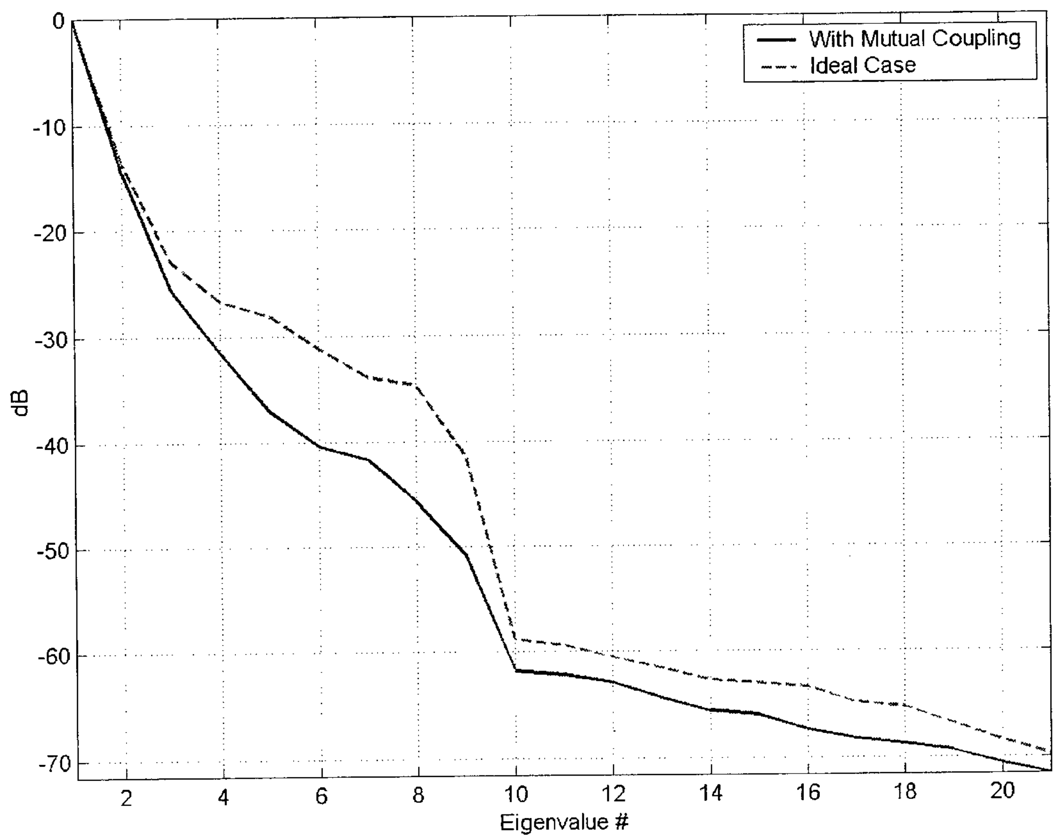

Figure 11: Eigenvalue spread with and without mutual coupling

2.3 Compensation for Mutual Coupling on the JDL Algorithm

As mentioned earlier, to minimize the computation load Wang and Cai [5] introduced the Joint Domain Localized (JDL) algorithm, a post-Doppler, beamspace approach that adaptively processes the radar data after transformation to the angle-Doppler domain. Adaptive processing is restricted to a

Localized Processing Region (LPR) in the transform domain, significantly reducing the DOF while retaining maximal gain against thermal noise. The reduced DOF leads to corresponding reductions in required sample support and computation load.

In developing the JDL algorithm, the authors assume the receiving antenna to be an equi-spaced linear array of ideal, isotropic, point sensors. Based on this assumption, space-time data is transformed to the angle-Doppler domain using a two dimensional Discrete Fourier Transform (DFT). This approach is valid under certain restrictions when the spatial and temporal steering vectors form the Fourier coefficients. Due to the orthonormality of the DFT, the look space-time steering vector is localized to a single point in the angle-Doppler domain.

The use of a 2D-DFT restricts the spacing between angle/Doppler bins and the possible look directions/velocities. Without zero padding, the DFT can form only N orthogonal angle beams and M orthogonal Doppler beams. If the look direction matches one of these N angle beams and the look Doppler matches one of these M Doppler beams, the look steering vector is a column of the 2D DFT matrix, which is orthogonal to the other columns of the matrix. The transformation therefore localizes the look steering vector to a single bin in the angle-Doppler domain. To maintain the localization of the target, the use of a window to suppress transform sidelobes is discouraged. For a small array, the beams corresponding to the columns of the DFT matrix are widely spaced in angle with correspondingly reduced "true" correlation between beams. For a large array, the beams are spaced too close together with little information gained with each additional beam resulting in very high beam to beam correlation.

When applying the JDL algorithm to measured data, a crucial assumption in the development of [5] is invalid. The elements of a real array cannot be point sensors. Due to their physical size, the elements of the array are subject to mutual coupling. Furthermore, the assumption of a linear array is restrictive. A planar array allows for degrees of freedom in azimuth and elevation. Therefore, the Fourier coefficients do not form the spatial steering vector and a DFT does not transform the spatial data to the angle domain. In this case, a DFT is mathematically feasible but has no physical meaning.

In a physical array, the spatial steering vectors must be measured or obtained using a numerical electromagnetic analysis. These steering vectors must be used to transform the space domain to the angle domain. This transformation is necessarily non-orthogonal with a corresponding spread of target information in the angle-Doppler domain. Earlier attempts to apply JDL to a real array ignored the non-orthogonal nature of the measured spatial transform [18].

Section 2 develops the JDL algorithm as applied to the case of an ideal array and serves to clarify the original development of the JDL algorithm as proposed by Wang and Cai [5]. The development is presented here to highlight the restrictions placed on the algorithm by the original formulation. Section 3 reformulates the JDL algorithm in terms of a transformation matrix. This formulation eliminates the restrictions on the JDL algorithm and the DFT based formulation becomes a special, not necessarily optimal, case. Section 4 presents examples to illustrate the improvement in processing performance obtained by the new formulation. The examples use simulated data for a linear array of isotropic sensors and measured data from the MCARM database [19].

2.3.1 Joint Domain Localized Processing

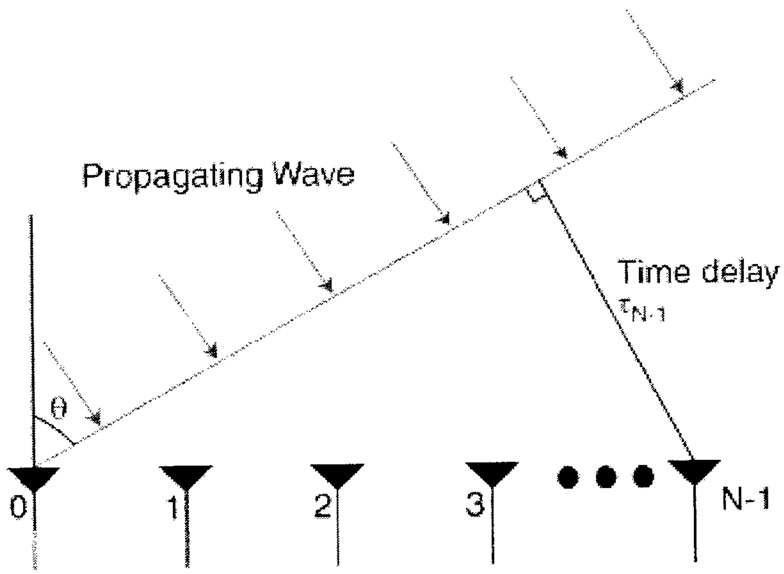

Figure 12: Linear array of point sensors

Consider an equispaced linear array of N isotropic, point sensors as shown in Figure 12. Note that the definition of incident angle is complementary to the definition in the earlier sections. Each channel receives M data samples corresponding to the M pulses in a CPI. Therefore, for each range bin the received data is a length MN vector **x** whose entries numbered mN to $[(m+1)N]$ correspond to the returns at the N elements in the array from pulse number m, where m=0,1, ... , M-1. The data vector is a sum of the contributions from the external interference sources, the thermal noise, and possibly a target,

$$\mathbf{x} = \xi \mathbf{s}(\phi, f_d) + \mathbf{c} + \mathbf{n}, \tag{20}$$

where ξ is the target amplitude, **c** the vector of interference sources and **n** the vector of white noise. The space-time steering vector **s** is defined in Eqn. (16). Note that in STAP the steering vector sets the look direction where the target *is assumed* to be. In practice, there is some beam mismatch between the real target return and the steering vector. Note that the spatial steering vector a(ϕ) is the magnitude and phase taper received at the N elements of the array due to a far field source at angle ϕ. Due to electromagnetic reciprocity, to transmit in the direction ϕ, the elements of the array must be excited with the conjugates of the steering vector, i.e. the conjugates of the steering vector maximize the response in the direction ϕ. Transformation of spatial data to the angle domain at angle ϕ therefore requires an inner product with the corresponding spatial steering vector. Similarly, the temporal steering $\mathbf{b}(f_d)$ vector corresponding to a normalized Doppler frequency f_d is the magnitude and phase taper measured at an individual element for the M pulses in a CPI. An inner product with the corresponding temporal steering vector transforms time domain data to the Doppler domain. The angle-Doppler response of the data vector **x** at angle ϕ and Doppler f_d is therefore given by

$$\tilde{x}(\phi, f_d) = \mathbf{s}^H(\phi, f_d)\mathbf{x} = \left[\mathbf{b}(f_d) \otimes \mathbf{a}(\phi)\right]^H \mathbf{x} \ , \tag{21}$$

where the tilde (˜) above the above the scalar x signifies the transform domain. Choosing a set of spatial and temporal steering vectors generates a corresponding vector of angle-Doppler domain data.

Equations (17) and (18) indicate that the for an ideal array, the temporal and spatial steering vectors are identical to the Fourier coefficients. Based on this observation, the transformation to the angle-Doppler domain can be simplified under two conditions:

- If a set of angles are chosen such that $[(d/\lambda)\sin\phi]$ is spaced by $1/N$ and a set of Doppler frequencies are chosen such that (f_d) is spaced by $1/M$, the transformation to the angle-Doppler domain is equivalent to the 2D DFT.
- If the look angle ϕ corresponds to one these angles and the look Doppler f_d corresponds to one of these Dopplers, the steering vector is a column of the 2D DFT matrix and the angle-Doppler steering vector is localized to a single angle-Doppler bin.

The JDL algorithm as originally developed in [5] assumes both these conditions are met. This simplification is possible only in the case of the ideal, equispaced, linear array of Figure 12. Due to beam mismatch, the localization to a single point in angle-Doppler space is only exact for the look steering vector.

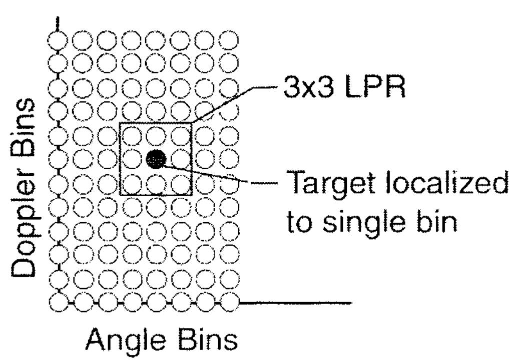

Figure 13: Localized Processing Regions in JDL

As shown in Figure 13, a LPR centered about the look angle-Doppler point is formed and interference is suppressed in this angle-Doppler region only. The LPR covers η_a angle bins and η_d Doppler bins. The choice of η_a and η_d is independent of N and M, i.e. the localization of the target to a single angle-Doppler bin decouples the number of adaptive degrees of freedom from the size of the data cube while retaining maximal gain against thermal noise. The covariance matrix corresponding to this

LPR is estimated using secondary data from neighboring range cells. The adaptive weights are then calculated by

$$\tilde{\mathbf{w}} = \tilde{\mathbf{R}}^{-1}\tilde{\mathbf{s}} \ , \tag{22}$$

where $\tilde{\mathbf{R}}$ is the estimated angle-Doppler covariance matrix corresponding to the LPR of interest. The number of adaptive unknowns is equal to $\eta_a\eta_d$ .The steering vector for the adaptive process is represented by $\tilde{\mathbf{s}}$ and is the space-time steering vector $\mathbf{s}$ transformed to the angle-Doppler domain. Under the two conditions listed above, $\tilde{\mathbf{s}}$ is given by the length $\eta_a\eta_d$ vector

$$\tilde{\mathbf{s}} = \begin{bmatrix} 0 \ 0 \cdots 0 \ 1 \ 0 \cdots 0 \ 0 \end{bmatrix}, \tag{23}$$

It must be emphasized that this simple form of the steering vector is valid only because the DFT is an orthogonal transformation and the space-time steering vector transformed to the angle-Doppler domain using the same transformation as used for the data. The adaptive weights of Eqn. (22) are used to find a statistic for detection by hypothesis testing. We use the embedded constant false alarm rate (CFAR) modified sample matrix inverse (MSMI) statistic

$$\rho_{MSMI} = \frac{\left|\tilde{\mathbf{w}}^H \tilde{\mathbf{x}}_{\mathrm{LPR}}\right|^2}{\tilde{\mathbf{w}}^H \tilde{\mathbf{s}}} \ , \tag{24}$$

where $\tilde{\mathbf{x}}_{\mathrm{LPR}}$ is the length $\eta_a\eta_d$ angle-Doppler data vector corresponding to the LPR and primary range bin.

2.3.2 JDL Based on a Transformation Matrix

As originally developed in [5], the JDL algorithm assumes a linear array of equispaced, isotropic, point sensors and the two conditions listed in Section 2.3.1. These conditions, though not explicitly stated in [5], restrict the choice of spacing between angle-Doppler bins in the transform domain and also the allowed look directions.

The most significant problem with the JDL algorithm described in Section 2.3.1 is that the assumption of an array of point sensors cannot be satisfied in practice. Each array element must have a non-zero physical size leading to mutual coupling between the elements. Furthermore, the assumption of a linear array is overly restrictive. Real arrays may be planar to allow for degrees of freedom in azimuth and elevation. In practice, the spatial steering vectors are not the Fourier coefficients given by Eqn. (18) and must be measured or obtained using a numerical electromagnetic analysis. The steering vectors so obtained can be used to transform the space domain to the angle domain. The continued use of a DFT is mathematically feasible, but the transform domain would not be the angle domain and would have no physical meaning.

In this section we replace the DFT based transformation described in Section 2.3.1 with a general transformation matrix. The key contribution of this new approach is the elimination of the two stipulations on the original JDL algorithm of Wang and Cai. This formulation can be directly applied to both linear arrays of isotropic point sensors and physical arrays of arbitrary configuration. In both cases, the modifications can result in significantly improved detection performance.

In the JDL algorithm, only data from within the LPR is used for the adaptation process. Equation (21) indicates that the transformation from the space-time domain to the angle-Doppler domain is, in effect, an inner product with a space-time steering vector. This argument holds true for ideal linear arrays *and* physical arrays. Mathematically therefore, the relevant transformation to within the LPR is a pre-multiplication with a $NM \times \eta_a\eta_d$ transformation matrix. The transformation process is

$$\tilde{\mathbf{x}}_{\mathrm{LPR}} = \mathbf{T}^H \mathbf{x}\ , \tag{25}$$

For example, based on Eqn. (21), if the LPR covers 3 angle bins $(\phi_{-1}, \phi_0, \phi_1, \eta_a = 3)$ and 3 Doppler bins $(f_{-1}, f_0, f_1, \eta_d = 3)$,

$$\begin{aligned}\mathbf{T} = [&\mathbf{b}(f_{-1}) \otimes \mathbf{a}(\phi_{-1})\ \ \mathbf{b}(f_{-1}) \otimes \mathbf{a}(\phi_0)\ \ \mathbf{b}(f_{-1}) \otimes \mathbf{a}(\phi_1)\\ &\mathbf{b}(f_0) \otimes \mathbf{a}(\phi_{-1})\ \ \mathbf{b}(f_0) \otimes \mathbf{a}(\phi_0)\ \ \mathbf{b}(f_0) \otimes \mathbf{a}(\phi_1)\\ &\mathbf{b}(f_1) \otimes \mathbf{a}(\phi_{-1})\ \ \mathbf{b}(f_1) \otimes \mathbf{a}(\phi_0)\ \ \mathbf{b}(f_1) \otimes \mathbf{a}(\phi_1)]\end{aligned} \tag{26}$$

$$= [\mathbf{b}(f_{-1})\ \ \mathbf{b}(f_0)\ \ \mathbf{b}(f_1)] \otimes [\mathbf{a}(\phi_{-1})\ \ \mathbf{a}(\phi_0)\ \ \mathbf{a}(\phi_1)].$$

In [5], to achieve the simple form of the angle-Doppler steering vector given by Eqn. (23), the use of a low sidelobe window to lower the transform sidelobes is discouraged. However a simple modification of the transformation matrix in Eqn. (26) allows for the use of a low sidelobe taper in the spatial and temporal domains. If a length N taper $\mathbf{t}_s$ is to be used in the spatial domain and a length M taper $\mathbf{t}_t$ is to be used in the temporal domain, the transformation matrix is given by

$$\mathbf{T} = [\mathbf{t}_t \bullet \mathbf{b}(f_{-1})\ \ \mathbf{t}_t \bullet \mathbf{b}(f_0)\ \ \mathbf{t}_t \bullet \mathbf{b}(f_1)] \otimes [\mathbf{t}_s \bullet \mathbf{a}(\phi_{-1})\ \ \mathbf{t}_s \bullet \mathbf{a}(\phi_0)\ \ \mathbf{t}_s \bullet \mathbf{a}(\phi_1)], \tag{27}$$

where $\bullet$ represents not the usual inner dot product, but the Hadamard product, a point-by-point multiplication of two vectors.

The angle-Doppler steering vector used to solve for the adaptive weights is given by the space-time steering vector (s) transformed to the angle-Doppler space *using the same transformation as used for the data,* i.e.

$$\tilde{\mathbf{s}} = \mathbf{T}^H \mathbf{s}. \tag{28}$$

Note the transformation matrix defined in Eqn. (26) is defined for the chosen Doppler frequencies and angles without any restrictions on their values. Further, no assumption is made about the form of the spatial or temporal steering vectors, i.e. the use of a transformation matrix eliminates the two restrictions placed on the original JDL formulation.

In the case of a linear array of isotropic point sensors, the steering vectors are obtained from Eqns. (17) and (18). If the angles and Doppler frequencies satisfy the conditions listed in Section 2.3.1, the transformation matrix **T** reduces to the relevant rows of the 2D DFT matrix. The DFT based formulation is equivalent to choosing a spacing in the angle domain such that $[(d/\lambda)\sin\phi = 1/N)$ and in the Doppler domain of $\Delta f = 1/M$. Furthermore, if both the look angle and Doppler corresponds to one of these angles and Dopplers, the transformed steering vector of Eqn. (28) is equivalent to the steering vector of Eqn. (23). Even in the ideal case of a linear array of isotropic point sensors, the formulation of [5] is therefore a special, not necessarily optimal, case of the more general formulation presented in this section.

The steering vector associated with a given angle is the measured magnitude and phase taper due to a calibrated far field source. If measurements are not available, the steering vectors can be obtained from a numerical electromagnetic analysis of the receiving antenna. Usually, even in the case of a real array, the pulses are equally spaced in time and hence the temporal steering vector is unchanged. In the case of a real array, the spatial component in Eqn. (18) must be replaced with a measured steering vector, i.e.

$$\mathbf{s}(\phi, f_d) = \mathbf{b}(f_d) \otimes \mathbf{a}_m(\phi), \tag{29}$$

with corresponding changes in the transformation matrix. The measured steering vector may also be obtained using a numerical electromagnetic analysis procedure, as in Section 2.1.1.

In Section 2.1.1, assuming both listed conditions are met and based on the orthogonality of the DFT, the target is localized to a single point in the angle-Doppler domain and the angle-Doppler steering vector reduces to the simple form in Eqn. (23). This simplification is invalid once the two restrictions are relaxed and the target information is spread in the angle-Doppler domain. The use of Eqn. (28) accounts for the resulting spread in target information.

Melvin and Himed [18] applied the JDL algorithm to measured data and used the measured steering vectors to transform the space domain to the angle domain. In effect, without explicitly stating so, they use a transformation matrix in the spatial domain and a DFT in the temporal domain. The spacing between the angles chosen for the LPR is determined by the available measured steering vectors. The spacing between the Doppler frequencies is fixed by the DFT. Crucially, the resulting change on the angle-Doppler steering vector $\tilde{\mathbf{s}}$ is ignored and they assume the simplified form of the steering vector in Eqn. (23) is valid. However, this is untrue since the use of a different transform from the spatial domain to the angle domain violates the assumptions on which Eqn. (23) is based. Furthermore, the authors of [13] explicitly discourage the use of low sidelobe tapers in the transformation.

The next section present four examples to illustrate the improvements in adaptive performance gained by using the transformation matrix formulation described above and taking the non-orthogonal nature of the spatial steering vectors in to account. The examples also illustrate the use of a windowed transformation from the space-time domain to the angle-Doppler domain. Two of the examples presented use simulated data based on an ideal linear array of point sensors. The other two examples use measured data from the Multi-Channel Airborne Radar Measurements (MCARM) [19] database.

2.3.3 Simulated Data

The formulation presented in Section 2.3.2 removed the restrictions placed by the original development of the JDL algorithm in [5]. This section presents two examples to illustrate the improvements in detection performance. The examples use simulated data based on an *ideal linear array of isotropic point sensors*. The detection performance is illustrated by plotting the probability of detection (P_d), obtained using a Monte Carlo simulation, as a function of the target signal-to-noise ratio for a chosen probability of false alarm (P_{fa}). The MSMI statistic of Eqn. (24) is used. This statistic has a constant false alarm rate (CFAR) in that, given Gaussian interference, P_{fa} is dependent only on the size of the covariance matrix, the number of secondary data vectors chosen to estimate the covariance matrix and the chosen threshold. In each of the examples presented, the P_d is evaluated for two cases: the DFT based JDL algorithm of [5] and the transformation matrix formulation presented above. The second case shows that the spacing between angle and Doppler bins in the transform domain are design variables that can be used to improve performance. Here, the spacing in angle domain is chosen to be a fraction of the spacing dictated by the DFT based formulation.

2.3.3.1 Data Model

These examples use a data cube containing the simulated returns of clutter and target information by an airborne linear array of isotropic point sensors. The data generation scheme uses the physical model presented by Jaffer *et.al.* [20] and Ward [4]. The clutter is modeled as a sum of the contributions of many discrete far field sources. In this example, 181 discrete sources are used, spaced 1^{o} apart. The amplitude of each source is a complex Gaussian random variable whose average power is set by a chosen clutter to noise ratio (CNR) and also weighted by the transmit beam pattern of the array. The normalized Doppler shift (f_c) associated with a clutter source at angle ϕ_c is set by the velocity of the array platform v_p and is given by

$$f_c = \beta \sin \phi, \tag{30}$$

where, as before, β is the number of half interelement spacings traversed by the aircraft in one pulse interval, i.e.

$$\beta = \frac{2}{d} \frac{v_p}{f_R}, \tag{31}$$

and f_R is the pulse repetition frequency. The contribution of the clutter patch at angle ϕ_c is therefore

$$\mathbf{c}(\phi_c) = \alpha[\mathbf{b}(f_c) \otimes \mathbf{a}(\phi_c)], \tag{32}$$

and α is the Gaussian random variable whose variance determines the CNR. The sum over all 181 clutter sources forms the overall received clutter vector.

The thermal noise is modeled as a Gaussian white noise process. The average power is set to unity allowing for the clutter and target powers to be referenced to the white noise power. These simulations do not include the effects of other interference sources such as jammers. In certain range cells, a target vector $\xi s(\phi, f_d)$ is added. The target amplitude ξ sets the signal to noise ratio.

The examples that use simulated data ignore other factors that effect STAP performance such as crab angle, mutual coupling and beam mismatch between target and steering vector. Table 6 lists the details of the array and interference scenario. The table also lists the parameters used in the implementation of the JDL algorithm and the spacing between angle and Doppler bins in the formulation of the modified JDL algorithm developed under this effort.

Table 6: Parameters for Examples 1 and 2.

Parameter	Example 1	Example 2
Elements (N)	8	8
Pulses (M)	8	8
Element Spacing	0.5 λ	10 λ
Pulse Repetition Frequency (f_R)	1024 Hz	1024 Hz
Mainbeam Transmit and Target Azimuth (ϕ)	0 deg	0 deg
Transmit Array Pattern	Uniform	Uniform
β	5.0	2.5
Target Normalized Doppler (f_d)	1/3	1/3
Thermal Noise Power	Unity	Unity
Clutter to Noise Ratio	50 dB	50 dB
Number of Angle bins in LPR	3	3
Number of Doppler bins in LPR	3	3
Angle bin spacing (modified JDL)	$1/2N$	$1/\sqrt{2}N$
Doppler bin spacing (modified JDL)	$1/2M$	$1/M$

2.3.3.2 Example 1: Half-Wavelength Spacing

This example uses data received by an 8-element array with 8 pulses per CPI. The spacing between array elements is $\lambda/2$. If one were using the DFT to transform the space domain to the angle domain, the spacing between angle bins is set automatically at $\Delta\sin\phi = (1/N)/(d/\lambda) = 1/(0.5N) = 0.25$, i.e. $\Delta\phi \approx 14.47''$. This large spacing leads to uncorrelated beams, reducing the ability of JDL to use the correlation to suppress interference. The new formulation uses 7.24'', i.e. half the spacing as the original JDL algorithm.

In this example, 36 secondary data vectors are used to estimate the 9×9 angle-Doppler covariance matrix. For the MSMI CFAR statistic, the threshold for a false alarm rate of 1% (P_{fa}=0.01) is 8.35. This high false alarm rate is chosen to reduce the number of trials required to obtain a reliable estimate of the probability of detection. The number of trials is chosen to be 9964.

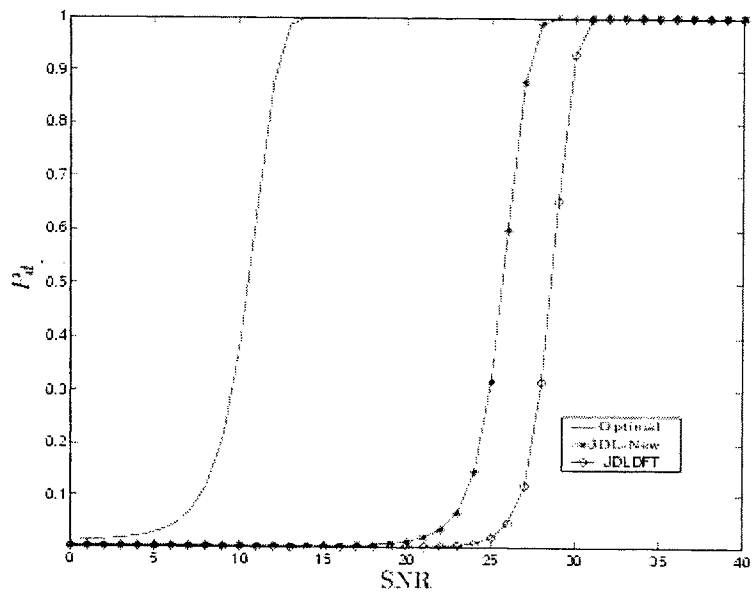

Figure 14: Example 1. Probability of detection versus Signal-to-Noise Ratio

Figure 14 plots the probability of detection versus the signal to noise ratio for the above threshold. The solid curve is the P_d using the optimal weights obtained using the known space-time covariance matrix. The other two curves compare the P_d using the formulation developed in this report with the P_d using the DFT-based JDL algorithm. As is seen, the probability of detection is significantly higher for the new formulation for the same signal-to-noise ratio and the same P_{fa}. The new formulation shifts the P_d curve to the left by approximately 4 dB, a significant improvement in detection performance.

2.3.3.3 Example 2. Large Inter-element Spacing

The second example illustrates the working of the new formulation using an array with a large interelement spacing of 10λ. The details of the array, the scenario, and the parameters used in the implementation of the JDL algorithm are listed in Table 6. Here the Doppler spacing chosen for the modified JDL algorithm is the same as in the case of using a DFT. As in Example 1, 9964 independent realizations are used to estimate the probability of detection.

Figure 15 plots the probability of detection versus the signal to noise ratio for the same threshold as in Example 1. The solid curve is the P_d using the optimal weights obtained using the known covariance matrix. The other two curves compare the P_d using the formulation developed in this report with the P_d

using the DFT-based JDL algorithm. For the same P_{fa}, the new formulation shifts the P_d curve to the left by approximately 2.5 dB.

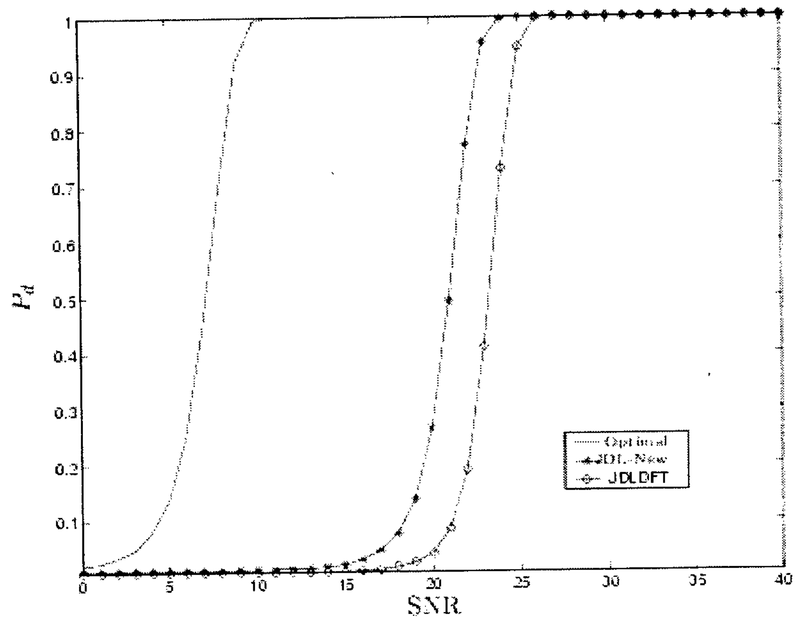

Figure 15: Example 2. Probability of detection versus Signal-to-Noise Ratio

It must be emphasized that this effort has investigated the optimal spacing between angle and Doppler bins to maximize the performance of the JDL algorithm. The spacings used here represent just one possible choice. The choice of the optimal spacing between angles and Doppler bins in the transform domain is an open research problem.

2.3.4 Measured Data: Using the MCARM Database

This section presents examples of the performance improvement gained using the formulation presented in this report, as applied to measured data. The examples use data from the Multi-Channel Airborne Radar Measurements (MCARM) database [19], a vast collection of clutter and signal measurements collected by an airborne radar over multiple flights with multiple acquisitions on each flight. The acquisitions used in these examples use a 22 element rectangular array arranged in a 2×11 grid ($N = 22$). Each CPI comprises 128 pulses (M=128).

The database includes clutter measurements over different terrain and the returns from a target aircraft flying approximately parallel to the radar platform. Some acquisitions include the signals (tones) from a Moving Target Simulator (MTS) of known Doppler shift and power. Also provided with the data is a set of measured spatial steering vectors for some specified azimuth and elevation angles. As explained in Section 2.3.2, these steering vectors are used in [18] and here for spatial processing of the data.

The two examples presented here illustrate the improvement in detection performance by accounting for the non-orthogonal nature of the steering vectors. For each example, three scenarios are compared. In the first two scenarios, the space-time data is transformed using a DFT in time and the measured steering vectors in space. The first scenario ignores the target spreading due to the non-orthogonal nature of the spatial steering vectors. This is equivalent to using Eqns. (25) and (26) to transform the space-time data to the angle-Doppler domain, but using Eqn. (23) as the angle-Doppler steering vector. This approach has been used by Melvin and Himed [19].

The second scenario accounts for the non-orthogonality and so uses Eqn. (28) to evaluate the angle-Doppler steering vector. The final scenario uses a window before transforming the time domain to Doppler domain. This scenario uses Eqn. (27) to evaluate the transformation matrix and Eqn. (28) to evaluate the adaptive steering vector for JDL. This effort has introduced, for the first time, the use of a window in the transformation. In all examples, 3 angle bins and 3 Doppler bins form the LPR. The spatial steering vectors are measured at approximately $1''$ spacings. The covariance matrix of the interference is estimated using 18 secondary data cells on either side of the range bin of interest neglecting the first range cell on each side as a guard cell, i.e. 36 secondary data vectors are used to estimate the angle-Doppler covariance matrix. The MSMI statistic of Eqn. (24) is used for detection.

In a radar system, a beam is transmitted in a particular direction and the returns are processed for targets in that direction only. Hence, while all Doppler frequencies of interest are examined, the angle bin of interest remains constant over the entire CPI. Therefore the adaptive steering vector of Eqn. (28) can be calculated {\it a-priori} for each CPI.

The performance of windowed JDL is sensitive to the choice of window. Harris compares the properties of many different possible windows [23]. His figure of merit is the difference between the equivalent noise bandwidth and the normalized 3-dB bandwidth of the window. Using this criterion, he concludes that for fixed point arithmetic, the Kaiser-Bessel window is the top performer. The sidelobes of the Kaiser-Bessel window can be controlled by a parameter κ which is half the time-bandwidth product of the window. In this work, we use a 128-point Kaiser-Bessel window with $\kappa=\log_{10}(128)$ in the time domain. In the space domain, due to the limited number of elements available, the reduction in the mainbeam gain is significant even for shallow windows. Hence, a window is not used in the space domain.

2.3.4.1 Example 1. Injected target

In the first example, a fictitious target of chosen amplitude, direction, and Doppler is added to the MCARM data at a particular range bin. The amplitude and phase taper of the injected target at each of the 22 channels is obtained from the measured steering vectors. The amplitude of the injected target is chosen such that it is too weak to be observed by non-adaptive digital beamforming. The JDL algorithm is used to detect the injected target by suppressing the clutter.

The JDL processing is performed at the target angle bin, for a few range bins surrounding the injected target, and for all Doppler bins. Since this example uses measured data, the figure of merit used to compare the three scenarios is the separation between the MSMI statistic at the target range/Doppler bin and the highest statistic at other range or Doppler bins. A large separation implies a large difference between target and residual interference, improving the ability to detect the target.

This example uses data from acquisition 575 on flight 5. The target parameters are:

- Amplitude (ξ) = $0.00003\angle 0^{o}$
- Angle Bin $= 0^{o} \equiv$ Broadside
- Doppler bin = -9
- Range bin = 290

Unfortunately, the MCARM database does not clearly define the noise level of the antenna. Different approaches to evaluating the noise level have yielded significantly varying results. For the acquisition at hand, the noise floor has been estimated between -81 and -95 dB. Therefore, the signal-to-noise ratio of the injected target before and after processing is not available.

Figure 16 plots the MSMI statistic, at the broadside and target range bin, as a function of Doppler for the first scenario where non-orthogonality between the steering vectors is ignored, i.e the ideal steering vector of Eqn. (23) is used for the adaptive processing. The statistic at the target location is clearly visible over the surrounding clutter. However, the target is found at Doppler bin -8, not the expected -9. The separation between the statistic at bin -8 and the highest clutter statistic at bin -24 is 3.13 dB. The statistic at Doppler bin -9 is actually lower than the surrounding clutter. Figure 17 plots the MSMI statistic as a function of range for Doppler bin -9. The target at range bin 290 is overwhelmed by the clutter at range bin 266 and the target is 8.73 dB below the clutter.

Figure 18 and Figure 19 show the same plots when the non-orthogonal nature of the spatial steering is accounted for. The improved detection performance is clearly visible with the peak in the correct Doppler bin of -9. The highest statistic at Doppler bin 53 is 8.39 dB below the statistic at the target. This is an improvement of 5.26 dB over the first scenario. Figure 19 plots the MSMI statistic as a function of range at the target Doppler for the second case. Note that accounting for the non-orthogonality of the steering vectors makes the target stand out over the surrounding clutter. The statistic at the target range 290 is 2.49 dB over the highest clutter statistic at range bin 266. This is an improvement of 11.22 dB over the first case.

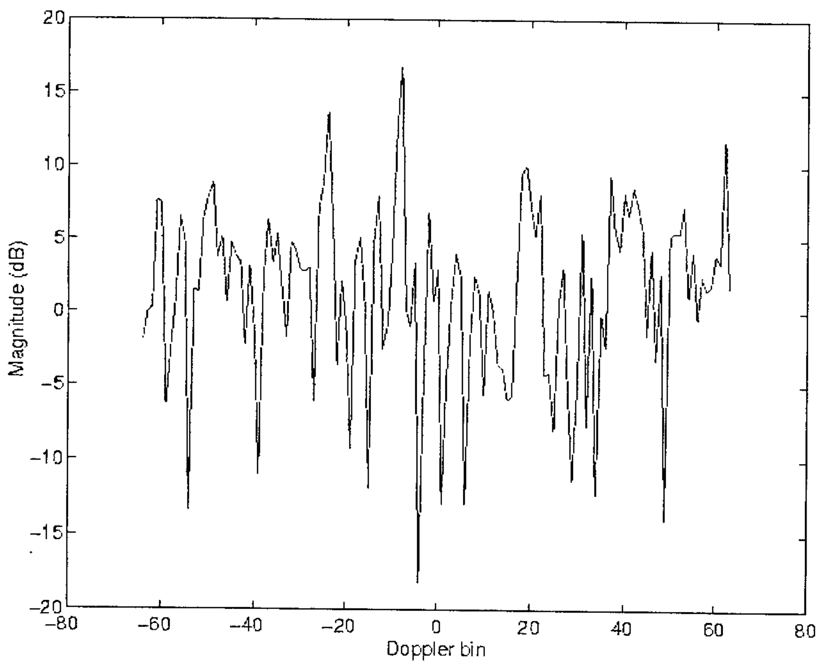

Figure 16: MSMI Statistic versus Doppler (Ignoring non-orthogonality of steering vectors)

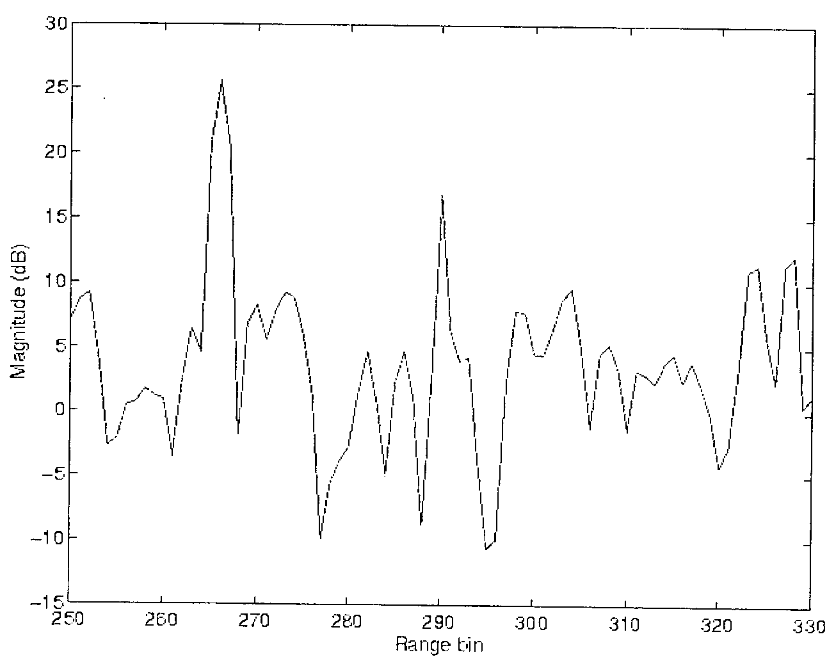

Figure 17: MSMI statistic versus range (Ignoring non-orthogonality of steering vectors)

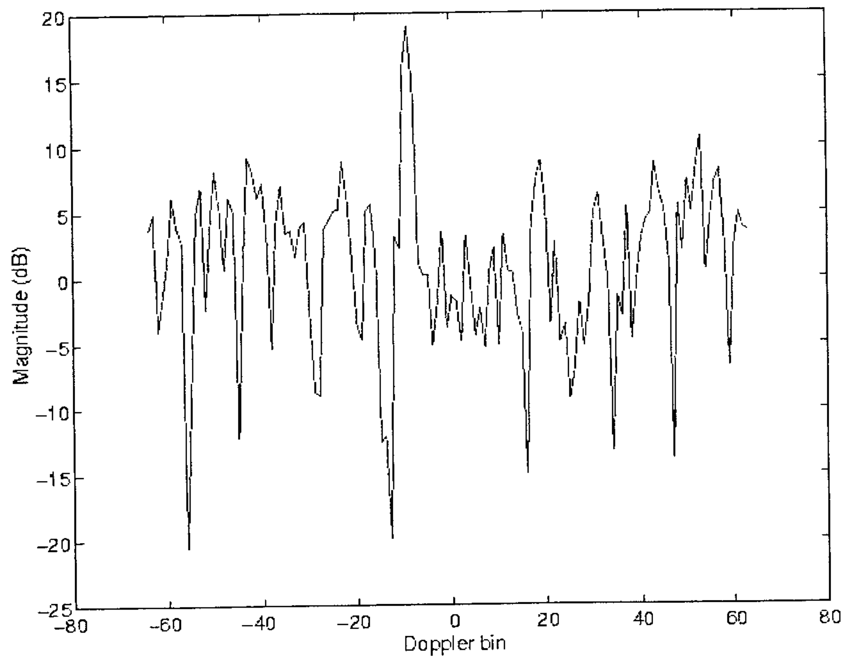

Figure 18: MSMI statistic versus Doppler (Accounting for non-orthogonality of steering vectors)

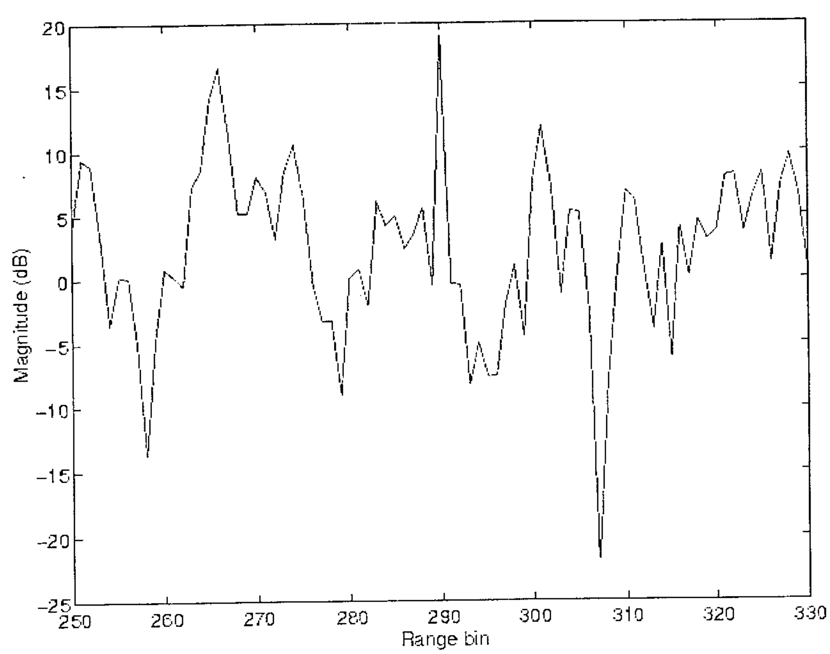

Figure 19: MSMI statistic versus Range (Accounting for non-orthogonality of steering vectors)

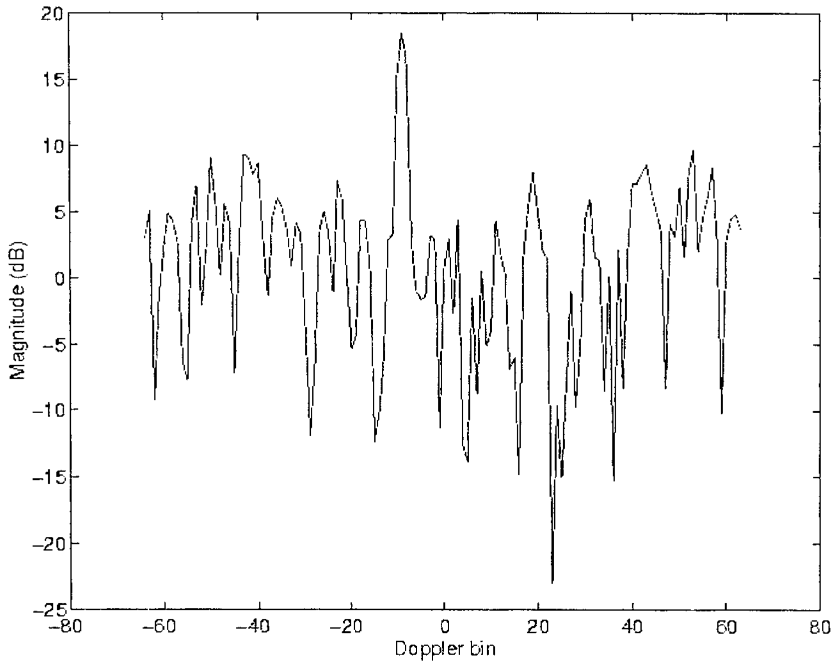

Figure 20: MSMI statistic versus Doppler. Using a Kaiser-Bessel window in transformation

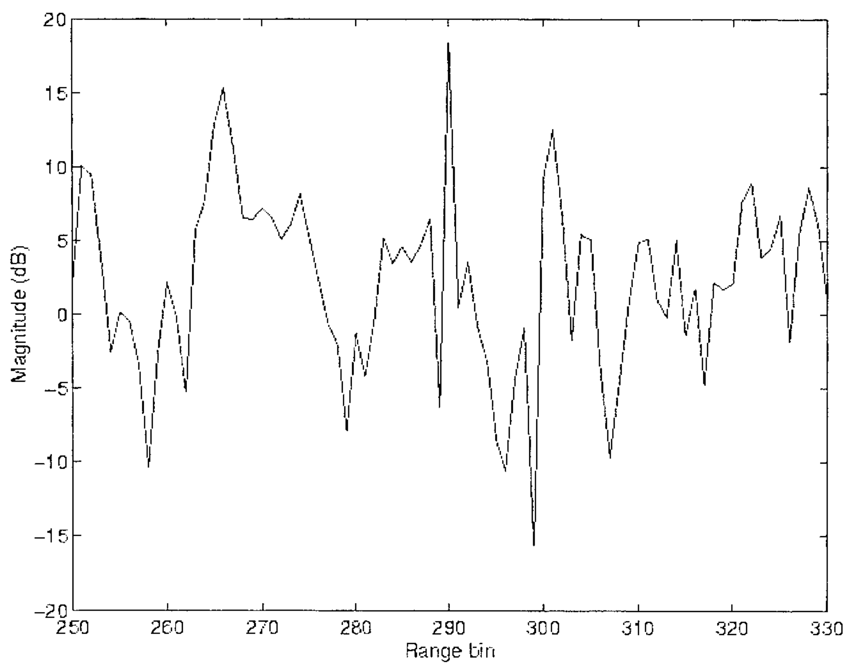

Figure 21: MSMI statistic versus Range. Using a Kaiser-Bessel window in transformation

Figure 20 plots the results when the Kaiser-Bessel window is used. The statistic is maximum at Doppler bin -9, showing a separation of 8.80 dB, an improvement of 5.67 dB over the first scenario and 0.41 dB over the second scenario. Figure 21 plots the results versus range. Again, the target, at range bin 290 stands out over the surrounding clutter. The separation over the highest clutter statistic is 3.13 dB, an improvement of 11.86 dB over the first scenario and 0.64 dB over the second scenario.

A summary of the results of the above figures Table 7. The improvement is listed with respect to traditional JDL processing.

Table 7: Separation between target and next highest MSMI statistic

Algorithm	Doppler	Improvement	Range	Improvement
JDL	3.10 dB	N/A	-8.73 dB	N/A
Modified JDL	8.39 dB	5.26 dB	2.49 dB	11.22 dB
JDL-Windowed	8.80 dB	5.67 dB	3.13 dB	11.86 dB

2.3.4.2 Example 2. MTS Tones

Flight 5 acquisition 152 includes clutter and tones from a moving target simulator (MTS) received at pre-selected Doppler frequencies. Five tones are received at approximately -800Hz (0 dB), -600 Hz (-14 dB), -400Hz (-20 dB), -200Hz (-26 dB) and 0~Hz (-31 dB). The data in this acquisition are the returns from 128 pulses measured at 22 channels. Using the Global Position System (GPS) and Inertial Navigation Unit data of the radar platform, the known location of the MTS source and the timing of the MTS pulse, it is possible to calculate the locations of the tones in range. The MTS generator is triggered by the transmit main beam and so the tones are in the transmit direction. For acquisition 152, the tones are located mainly in range bin 450 and about 6″ degrees towards the nose. The pulse repetition frequency for this flight was 1984 Hz, hence the separation of 200 Hz corresponds to nearly 13 Doppler bins.

Using the acquisition with the MTS tones allows us to compare the performance of the JDL algorithm in the above scenarios on real data without any injected targets. The tones act as returns from moving targets. The presence of five MTS tones makes it difficult to define a single figure of merit to compare the different scenarios and so a visual inspection is used for comparison.

Figure 22 plots the results of using a non-adaptive digital beamformer to locate the MTS tones in Doppler at the range bin and angle of the transmitter. The strongest tones at Doppler bins –52 and -39 are clearly visible over the clutter. The other three tones are visible but embedded in the surrounding clutter.

Figure 23 plots the results of using the JDL algorithm without accounting for the non-orthogonality of the steering vectors. As can be seen, the five MTS tones are visible, with the strongest tone at bin -53 spread out over Doppler space. However, a few spurious tones are also seen.

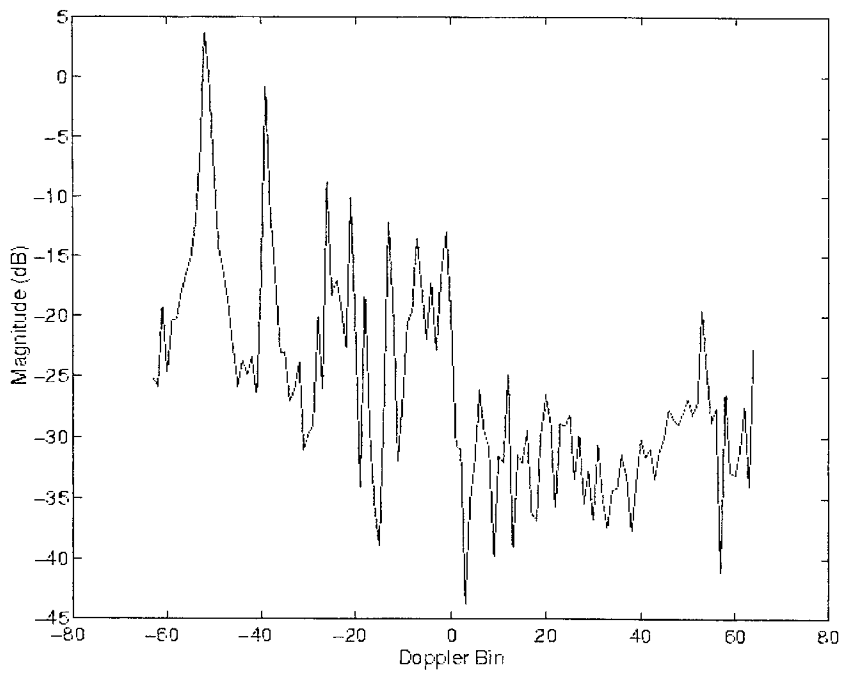

Figure 22: Location of the MTS tones using a non-adaptive beamformer

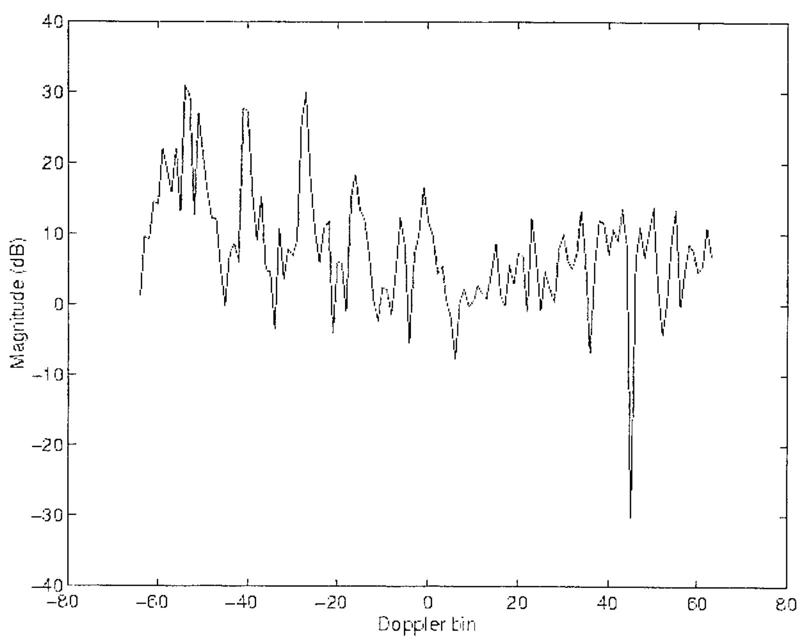

Figure 23: Detection of MTS Tones ignoring the non-orthogonality of the steering vectors

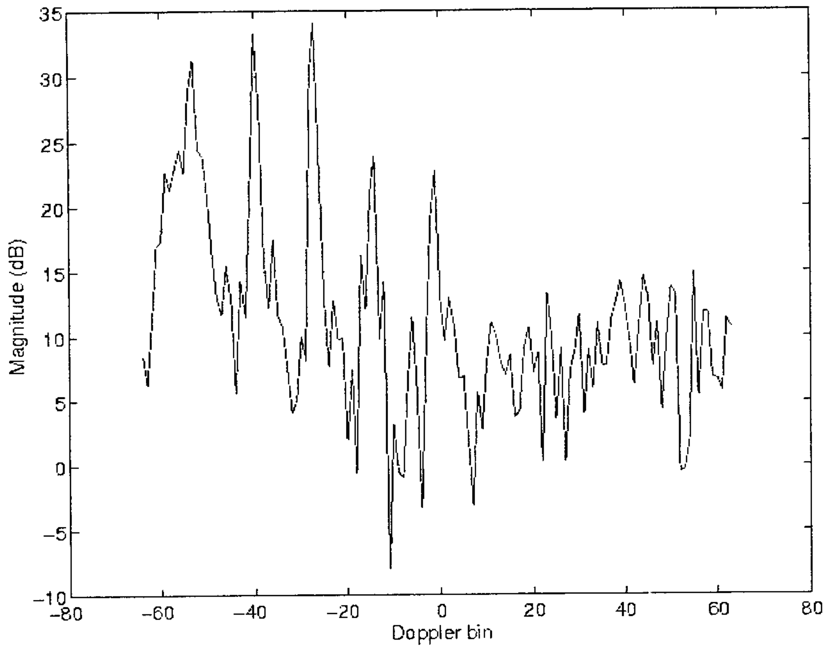

Figure 24: Detection of MTS Tones accounting for the non-orthogonality of the steering vectors

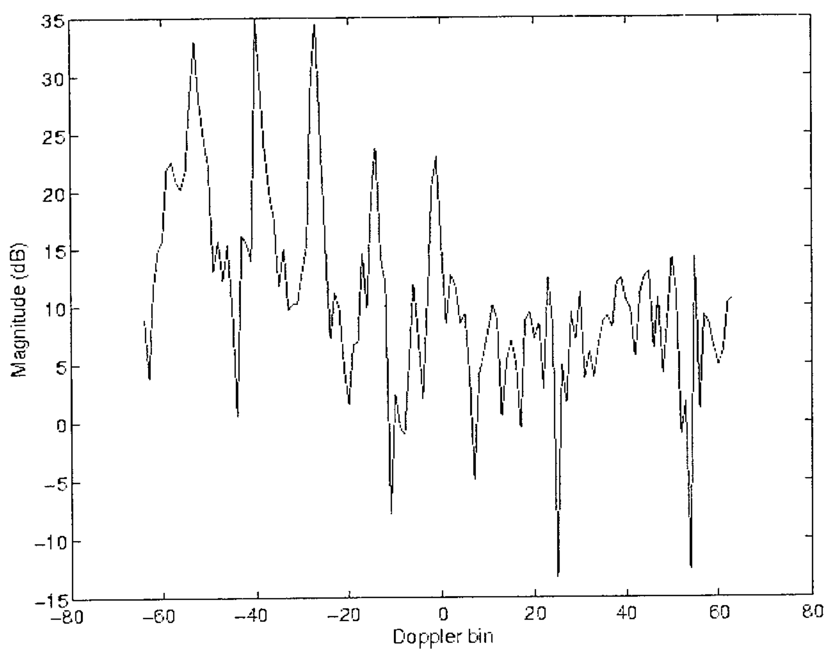

Figure 25: Detection of MTS Tones using a Kaiser-Bessel window

Figure 24 plots the results of taking the non-orthogonality of the measured steering vectors into account. The five MTS tones all clearly stand out over the clutter and the spread of the strongest tone has been curtailed. The spurious tones are completely suppressed. Figure 25 plots the case where the Kaiser-Bessel window is used to transform the time domain to the Doppler domain. Again, the five tones clearly stand out and the spread of the strongest tone is curtailed. This case shows some improvement over the case of Figure 24.

2.4 Conclusions Regarding Mutual Coupling

This theme of this effort is the transition of STAP algorithms from theory to practice, i.e the theme of this effort is to develop the theoretical foundations to deal with real world effects ignored in the original formulations. One of the most important real world effect that has been long ignored is the mutual coupling between the elements of the antenna array. Sections 2.1 and 2.2 present the impact of mutual coupling on the performance of direct data domain (Section 2.1) and statistical algorithms (Section 2.2). Equally importantly, the two sections present simple, effective techniques to compensate for mutual coupling in both D^3 and statistical cases.

For the development of practical direct data domain algorithms, the electromagnetic nature of the array must be taken into account. This effort has shown that the mutual coupling between the elements of the array causes adaptive algorithms to fail. This problem is associated with both covariance matrix approaches (stated earlier by Gupta and Ksienski [8]) and direct data domain approaches (investigated here).

To properly characterize the antenna, the Method of Moments is used. Previously published work in this area has used only one basis function per element, equivalent to using open circuit voltages. However, this is usually inadequate for an accurate antenna analysis. The use of multiple basis functions per element in a practical manner is a major advance over previously published methods. The mutual coupling is eliminated by recognizing that the MOM voltage vector is free from mutual coupling. By using a relationship between the entries of the MOM voltage vector, a square matrix equation is developed between the given measured voltages and the relevant entries of the MOM voltage vector. It is shown that this method works very well in the presence of strong interfering sources. Furthermore, it is shown that the proposed technique is superior to the earlier suggested method of using the open circuit voltages.

In the realm of statistical processing, the JDL processing algorithm, as originally developed by Wang and Cai [5], transforms space-time data to the angle-Doppler domain using a 2D DFT. The DFT based transformation restricts look angles and the spacing between the angle-Doppler bins in the transform domain. These restrictions are not stated explicitly in the original presentation. Furthermore, in practice, the spatial steering vector is affected by mutual coupling between the elements of the array. The DFT is not the appropriate transform from the space domain to the angle domain. In a practical case, spatial data must be transformed to the angle domain using an inner product with the corresponding measured steering vector. The spatial transformation is necessarily non-orthogonal leading to spreading of target information in the angle domain.

This effort has reformulated the JDL algorithm in terms of a general transformation matrix encompassing both the theoretical and practical scenarios. The formulation removes the restrictions placed on the original JDL algorithm. Removing the restrictions on spacing between angle and Doppler bins significantly improves the performance of the JDL algorithm. Section 2.2 uses two examples to illustrate the improvement in the probability of detection for a given false alarm rate. These examples use simulated data from an ideal array of point sensors. This allows for enough independent realizations for a reasonable Monte Carlo simulation. It must be emphasized that the choice of optimal spacing between angle and Doppler bins is yet an open research problem.

This report has also presented examples to illustrate the improvement in adaptive processing using measured data from the MCARM program. While earlier researchers have used measured steering vectors for the spatial transformation, the resulting spread in target information had been ignored. The formulation presented here accounts for the spread and yields significantly improved performance.

This effort has also introduced, for the first time, a window in the transformation from the space-time domain to the angle-Doppler domain. In earlier publications on the JDL algorithm, the use of a window is explicitly discouraged because of the resulting spread in target information. However, since any target spread can be accounted or, it is possible to take advantage of the low transform sidelobes by using an appropriate window.

The key contribution of this new approach is the elimination of the two stipulations on the original JDL algorithm and the introduction of a matrix based transformation to the angle-Doppler domain. Interestingly, the investigation of the impact of mutual coupling on the JDL algorithm has also resulted in improvements in performance in the purely theoretical scenario of an ideal array of point sensors.

In summary, this effort has investigated a topic that is very important to the development of practical adaptive algorithms. The proposed methods are easy to implement and do not add an inordinate computational burden on the adaptive process. The next section presents another important aspect of the transition from theory to practice: how non-homogeneous impacts on the performance of statistical STAP algorithms.

3.0 Nonhomogeneous Data

This section presents another of the key issues that limit the performance of adaptive processing algorithms in real world applications: the non-homogeneous and dynamic background environments typically observed from airborne radar. Non-homogeneous data is the most significant of the three issues that we discuss. Significant processing losses result from mismatches between the environment and the processing algorithms.

3.1 Direct Data Domain Processing

The inability of traditional statistical algorithms to counter the non-homogeneous component of interference motivates research in non-statistical or direct data domain (D^3) algorithms.

As described in Section 2.1.2.1, in [6] an algorithm is developed that optimizes the signal to interference in a least squares sense for signals at the angle at which a look-direction constraint is established. This method minimizes, in a least squares sense, the error between the received voltages (signal plus interference) and a signal from the assumed angle. This approach does not employ data from outside the radar range cell being evaluated, i.e. this approach does not require secondary data. This makes the D^3 an attractive alternative in non-homogeneous clutter. This is especially true in a severely non-homogeneous clutter environment of urban and land/sea interfaces. The D^3 approach has recently focused on one-dimensional spatial adaptivity [6]. This section introduces a new two-dimensional space-time D^3 algorithm based on the one-dimensional algorithm of [6].

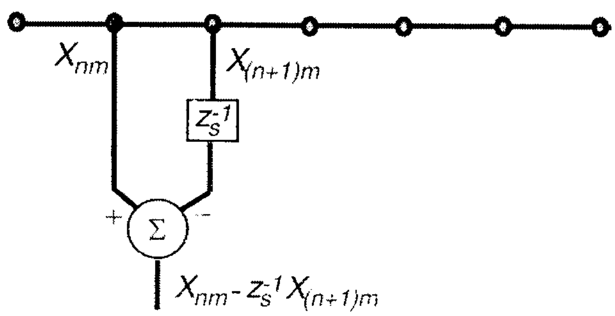

Figure 26: Principle of Direct Data Domain Processing

Consider the N-element uniformly spaced array shown in Figure 26. For a look direction of ϕ_s, the signal advances from one element to the next by the same phase factor $z_s=[\exp(j2\pi\sin(\phi_s))]$. The term obtained by the subtraction operation in Figure 26 is *therefore free of the target signal and contains only interference terms.* The D^3 algorithm minimizes the power in such interference terms while maintaining gain in the direction of the target.

To best present the D^3 algorithm, the data from the N elements due to the M pulses in a CPI is written as a $N \times M$ matrix $\mathbf{X}$ whose m^{th} column corresponds to the N returns from the m^{th} pulse, represented by $\mathbf{x}(m)$. The data matrix is a sum of target and interference terms. Rewriting Eqn. (6) in terms of matrices

$$\mathbf{X} = \xi \mathbf{S}(\phi, f_d) + \mathbf{C} + \mathbf{N}. \tag{33}$$

Define the $M \times (N\text{-}1)$ matrix **A** to be

$$\mathbf{A} = \begin{bmatrix} \mathbf{X}_{00} - z_s^{-1}\mathbf{X}_{10} & \mathbf{X}_{10} - z_s^{-1}\mathbf{X}_{20} & \cdots & \mathbf{X}_{(N-2)0} - z_s^{-1}\mathbf{X}_{(N-1)0} \\ \mathbf{X}_{01} - z_s^{-1}\mathbf{X}_{11} & \mathbf{X}_{11} - z_s^{-1}\mathbf{X}_{21} & \cdots & \mathbf{X}_{(N-2)1} - z_s^{-1}\mathbf{X}_{(N-1)1} \\ \vdots & \vdots & \vdots & \vdots \\ \mathbf{X}_{0(M-1)} - z_s^{-1}\mathbf{X}_{1(M-1)} & \mathbf{X}_{1(M-1)} - z_s^{-1}\mathbf{X}_{2(M-1)} & \cdots & \mathbf{X}_{(N-2)(M-1)} - z_s^{-1}\mathbf{X}_{(N-1)(M-1)} \end{bmatrix}, \quad (34)$$

where z_s, as defined earlier, is the phase progression of the *target signal* from one element to the next. Theoretically, the entries of **A** are interference terms only, though due to beam mismatch there may be some residual signal power. However, unless the target is significantly off the look direction/Doppler, the target signal is effectively nulled. In case the target is significantly off the look direction, it must be treated as interference: in a surveillance radar, targets must be declared only if they are in the look direction. In fact, sidelobe targets are an example of the discrete, non-homogeneous, interference that drives this research.

Consider the following two scalar functions of a vector of spatial weights $\mathbf{w}_s$.

$$\begin{aligned} G_{\mathbf{w}_s} &= \left|\mathbf{w}_s^H \mathbf{a}_{(0:N-2)}\right|^2 = \mathbf{w}_s^H \mathbf{a}_{(0:N-2)} \mathbf{a}_{(0:N-2)}^H \mathbf{w}_s, \\ I_{\mathbf{w}_s} &= \left\|\mathbf{A}^* \mathbf{w}_s\right\|^2 = \mathbf{w}_s^H \mathbf{A}^T \mathbf{A}^* \mathbf{w}_s, \\ R_{\mathbf{w}_s} &= G_{\mathbf{w}_s} - \kappa^2 I_{\mathbf{w}_s}, \end{aligned} \quad (35)$$

where $\|\cdot\|$ represents the 2-norm of a vector and $\mathbf{a}_{(0:N-2)}$ represents the first N-1 entries of the spatial steering vector. In the equation, $\mathbf{A}^*\mathbf{w}_s$ is used to remain consistent with the term $\mathbf{w}_s^H\mathbf{a}_{(0:N-2)}$ in that the weights multiply the conjugate of the data.

The term G in Eqn. (35) represents the gain of the weight vector $\mathbf{w}_s$ at the look angle ϕ_L while the term I represents the residual interference power after the data is filtered by the same weights. Hence, the term R is the difference between the gain of the antenna at the look Doppler and the residual interference power. The term κ in the definition of R is an emphasis parameter that will be described later. The D^3 algorithm finds the weights that maximize this difference. Mathematically,

$$\begin{aligned} \max_{\|\mathbf{w}_t\|_2 = 1} [\mathrm{R}_{\mathbf{w}_t}] &= \max_{\|\mathbf{w}_t\|_2 = 1} \left[G_{\mathbf{w}_t} - \kappa^2 I_{\mathbf{w}_t}\right], \\ &= \max_{\|\mathbf{w}_t\|_2 = 1} \mathbf{w}_t^H \left[\mathbf{a}_{(0:N-2)} \mathbf{a}_{(0:N-2)}^H - \kappa^2 \mathbf{A}^T \mathbf{A}^*\right] \mathbf{w}_t, \end{aligned} \quad (36)$$

where the constraint $\|\mathbf{w}_s\|_2 = 1$ is chosen to obtain a finite solution. Using the method of Lagrange multipliers, it can be shown that the desired temporal weight vector is the eigenvector corresponding to the maximum eigenvalue of the $(N\text{-}1) \times (N\text{-}1)$ matrix $\left[\mathbf{a}_{(0:N-2)} \mathbf{a}_{(0:N-2)}^H - \kappa^2 \mathbf{A}^T \mathbf{A}^*\right]$. This formulation yields a spatial weight vector of length (N-1). The loss of one DOF represents the subtraction operation in defining the entries of $\mathbf{A}$.

Analogous to the spatial adaptive weights, the temporal weight vector $\mathbf{w}_t$ is the eigenvector corresponding to the largest eigenvalue of the (M-1)×(M-1) matrix $\left[\mathbf{b}_{(0:M-2)}\mathbf{b}^H_{(0:M-2)} - \kappa^2\mathbf{B}^T\mathbf{B}^*\right]$, where $\mathbf{b}_{(0:M-2)}$ is the vector of the first (M-1) entries of the temporal steering vector defined by Eqn. (17) and $\mathbf{B}$ is the N×(M-1) matrix

$$\mathbf{B} = \begin{bmatrix} \mathbf{X}_{00} - z_t\mathbf{X}_{01} & \mathbf{X}_{01} - z_t\mathbf{X}_{01} & \cdots & \mathbf{X}_{0(M-2)} - z_t\mathbf{X}_{0(M-1)} \\ \mathbf{X}_{10} - z_t\mathbf{X}_{11} & \mathbf{X}_{11} - z_t\mathbf{X}_{12} & \cdots & \mathbf{X}_{1(M-2)} - z_t\mathbf{X}_{1(M-1)} \\ \vdots & \vdots & \vdots & \vdots \\ \mathbf{X}_{(N\text{-}1)0} - z_t\mathbf{X}_{(N\text{-}1)1} & \mathbf{X}_{(N\text{-}1)1} - z_t\mathbf{X}_{(N\text{-}1)2} & \cdots & \mathbf{X}_{(N-1)(M-2)} - z_t\mathbf{X}_{(N-1)(M-1)} \end{bmatrix} \tag{37}$$

The length NM space-time adaptive weight vector, for look angle ϕ and look Doppler f_d is then given by

$$\mathbf{w}(\phi, f_d) = \begin{bmatrix} \mathbf{w}_t \\ 0 \end{bmatrix} \otimes \begin{bmatrix} \mathbf{w}_s \\ 0 \end{bmatrix}. \tag{38}$$

The zeros appended to the spatial and temporal weight vectors represent the lost DOF in space and time.

The parameter κ above sets a trade off between mainbeam gain and interference suppression. By changing the value of this parameter, it is possible to emphasize one or the other term. In determining the spatial weights, choosing $\kappa = 0$ eliminates the interference term leaving the largest eigenvalue equal to $\left\|\mathbf{a}_{(0:N-2)}\right\|_2^2 = (N-1)$ with the corresponding eigenvector $\mathbf{w}_s = \mathbf{a}_{(0:N-2)} / \left\|\mathbf{a}_{(0:N-2)}\right\|_2$. Therefore, as $\kappa \to 0$ the D^3 weight vector approaches the non-adaptive steering vector used in pulse-Doppler processing.

On the other hand, if κ is chosen to be large, the role of the gain term G is negligible and the weight vector is dependent on the interference terms only. This leads to emphasis on the suppression of interference at the expense of mainbeam gain. In this case, the look direction plays a limited role through the term z_s and the weight vector may vary significantly by range cell.

Note that the adaptive weight vector in Eqn. (38) is obtained using data from the *primary range cell only*. There is no estimation of a covariance matrix and no correlation information required to obtain the adaptive weights. This property gives direct data domain processing its greatest advantage and its greatest disadvantage. The lack of an estimation of correlation allows use of D^3 processing in severely non-homogeneous situations. However, ignoring correlation information limits its ability to suppress correlated interference. A hybrid method to overcome this drawback and combine the benefits of statistical and non-statistical (D^3) processing will be described in Section 3.2.

3.1.1 Performance of D^3 Algorithm in Non-homogeneous Interference

This section presents a simulation to illustrate the advantages and disadvantages of D^3 processing. This simulation includes the effects of clutter, barrage noise jammers, white noise and a discrete interferer. Table 8 lists the parameters used in the example. The jammer and discrete interferer powers are referenced to the noise level. The clutter power is fixed by the transmit power and the assumed land reflectivity. The clutter and jammers represent correlated interference because these two interfernece sources are homogeneous across all range cells. Note that the discrete interferer is within the target range cell only, with an offset from the look direction in angle but not Doppler. Matching the non-homogeneity to the target in one domain makes it more difficult for the D^3 algorithm to suppress the non-homogeneity.

Table 8: Parameters for example using simulated data

Parameter	*Value*	*Parameter*	*Value*
Elements (N)	18	Pulses (M)	18
Element Spacing	0.5λ	Pulse repetition frequency	300 Hz
Array Transmit Pattern	Uniform	Uncompressed pulse width	400μs
Mainbeam Transmit Azimuth	0 deg	Transmit power	400kw
Backlobe attenuation	30	Land reflectivity	-3.0dB
Jammer azimuth angles	[-20° 45°]	Jammer powers	[40 dB 40 dB]
Target normalized Doppler (f_t)	1/3	Jammer Elevation angles	[0° 0°]
Doppler of interferer	1/3	Interferer power	40 dB
Angle of interferer	-51°	Thermal noise power	Unity
β (Clutter slope)	1	Number of clutter patches	361

The adapted beam pattern plots presented in this report are the mean patterns over 200 independent realizations. Vertical bars represent the standard deviation over these 200 trials. This method was required because the D^3 algorithm is non-statistical and based solely on a single data set/realization. Operating with the known covariance matrix to obtain an ideal pattern, as possible in statistical algorithms, is not an option.

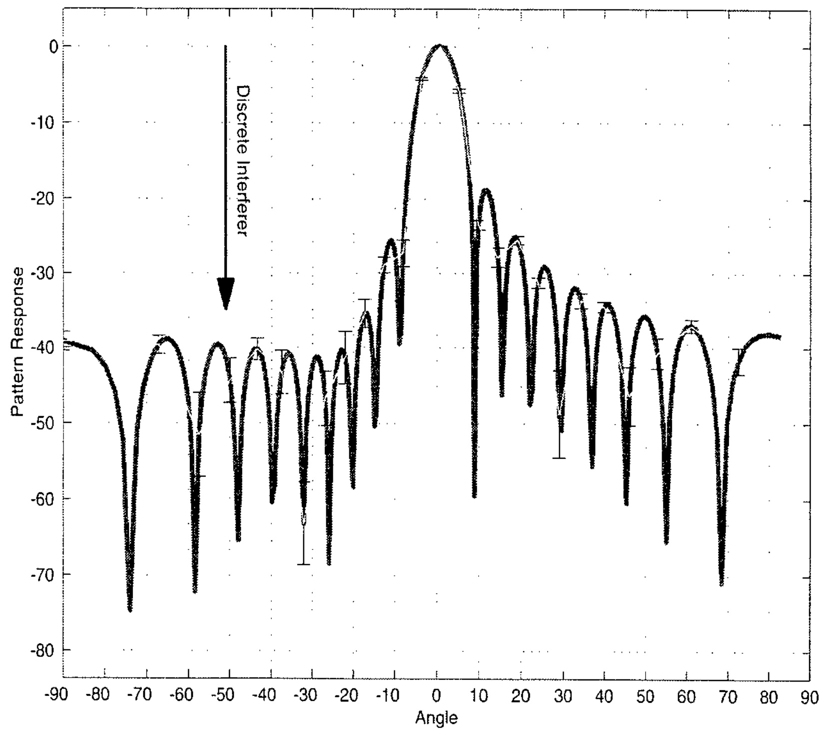

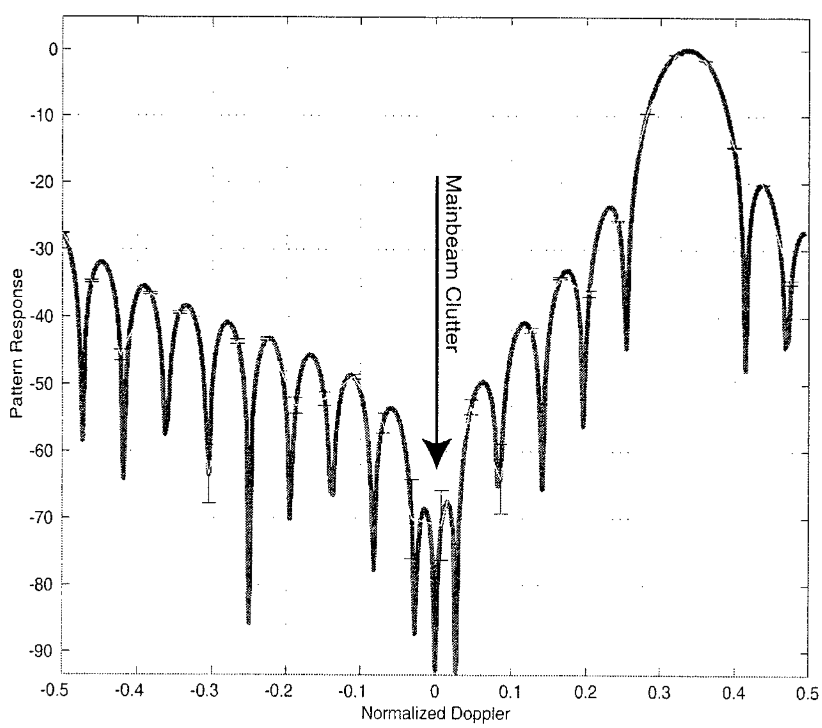

Figure 27: JDL Antenna Patterns at Target Doppler and Azimuth
(a) Angle Pattern (b) Doppler Pattern

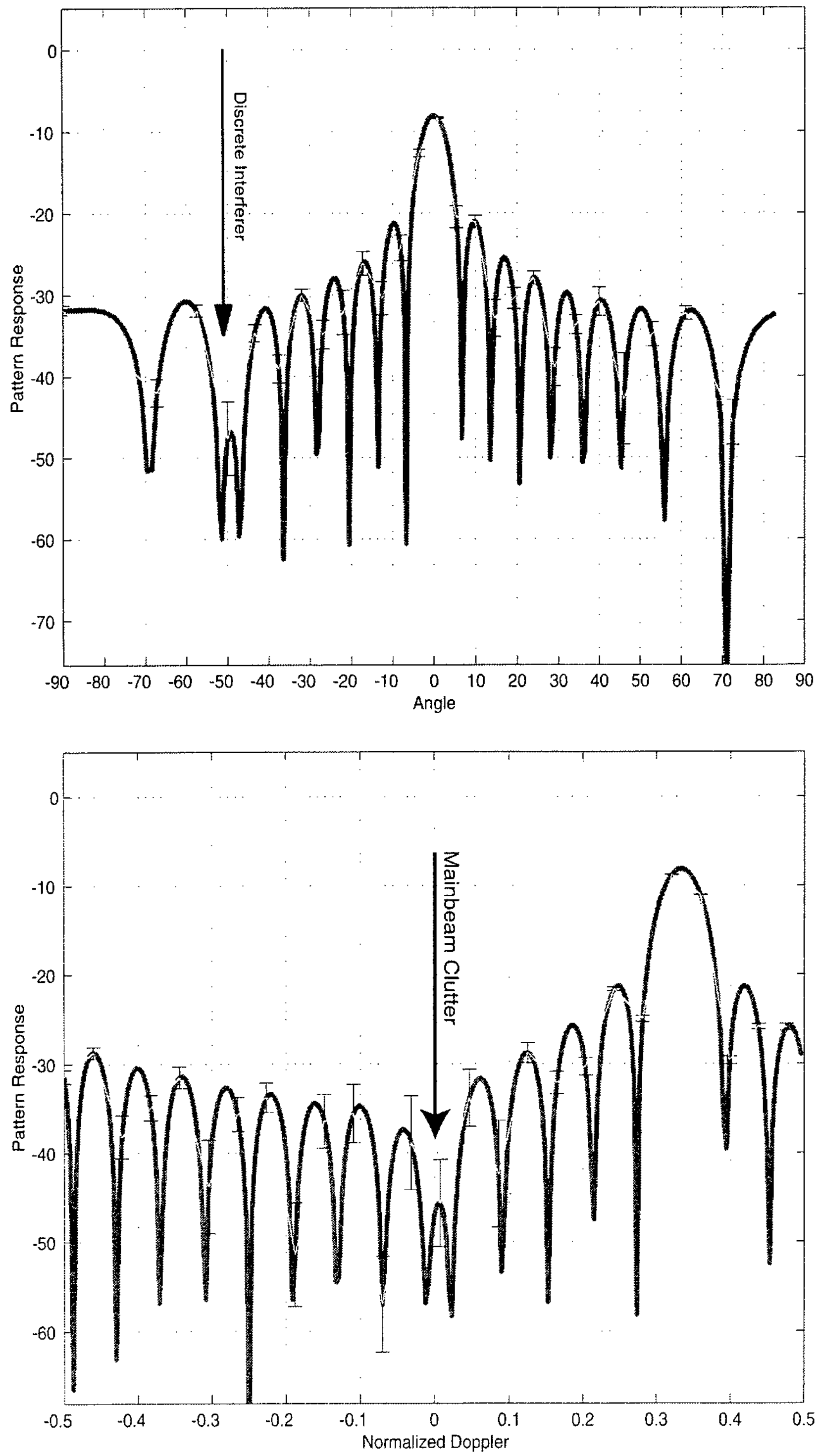

Figure 28: Direct Data Domain Patterns at Target Doppler and Azimuth

(a) Angle Pattern (b) Doppler Pattern

Figure 27 illustrates the antenna patterns along the target azimuth and Doppler for the JDL algorithm. In the angle plot, note the high sidelobe in the direction of the discrete interferer. The discrete interferer is within the primary range cell and so does not contribute to the covariance matrix estimate and therefore *cannot* be nulled by a purely statistical algorithm such as JDL. However, the angle plot shows the JDL algorithm does place deep nulls in the direction of the white noise jammers at -20° and 45°. The Doppler plot shows the deep null placed at zero Doppler frequency corresponding to mainbeam clutter. These two figures illustrate the effectiveness of the JDL algorithm in suppressing correlated interference such as jamming and clutter. However, they also illustrate the inability of a purely statistical algorithm to suppress point non-homogeneities (discretes).

Figure 28 plots the antenna patterns resulting from the implementation of the two-dimensional D^3 algorithm. The angle plot shows that the D^3 algorithm places a null in the direction of the discrete interferer. The adapted spatial beam pattern shows a distinct null in the direction of the discrete interferer at –51°, i.e. the algorithm is effective in countering a discrete interferer within the range cell of interest. However, the figure also illustrates the limitations of the D^3 algorithm. The nulls in the direction of the jammers are not as deep as in the case of JDL. The Doppler plot shows a shallow null in the direction of the mainbeam clutter. In summary, D^3 algorithms do not suppress correlated interference as well as statistical algorithms, however they are an excellent processing technique to deal with non-homogeneities. In the next section, we present results from combining the benefits of D^3 and statistical algorithms.

3.2 Hybrid Processing

Performance degradation of STAP algorithms due to non-homogeneous data occurs in two forms. In one form the secondary data is not i.i.d., leading to an inaccurate estimate of the covariance matrix. For example, the clutter statistics in urban environments fluctuate rapidly with range. To minimize the loss in performance due to non-homogeneous sample support, a NHD may be used to identify secondary data cells that do not reflect the statistical properties of the primary data. These data samples are then eliminated from the estimate of the covariance matrix.

The second form of performance loss is due to a discrete non-homogeneity within the primary range cell. For example, a large target within the test range cell but at a different angle and/or Doppler appears as a false alarm at the look angle-Doppler domain. Other examples include a strong discrete non-homogeneity, such as a corner reflector, in the primary range cell. These false alarms appear through the sidelobes of the adapted beam pattern. The secondary data cells do not carry information about the discrete non-homogeneity and hence a statistical algorithm cannot suppress discrete (uncorrelated) interference within the range cell under test. The example presented in Section 3.1.1 illustrates the impact of such a non-homogeneity.

The inability of statistical STAP algorithms to counter non-homogeneities in the primary data motivates research in the area of non-statistical D^3 algorithms, such as that described in Section 3.1.

These algorithms use data from the range cell of interest only, eliminating the sample support problems associated with statistical approaches.

The main contribution of this section is the introduction of a two-stage hybrid STAP algorithm combining the benefits of both non-statistical and statistical methods. The hybrid approach uses the non-statistical algorithm of Section 3.1 as a first-stage filter to suppress discrete interferers present in the range cell of interest. This first stage serves as an *adaptive transform* from the space-time domain to the angle-Doppler domain and is followed by JDL processing in the second stage. The adaptive transform replaces the steering vector based non-adaptive transform used in Section 2.3.2. The second stage is designed to filter out the residual correlated interference [23].

3.2.1 Two-Stage Hybrid Algorithm

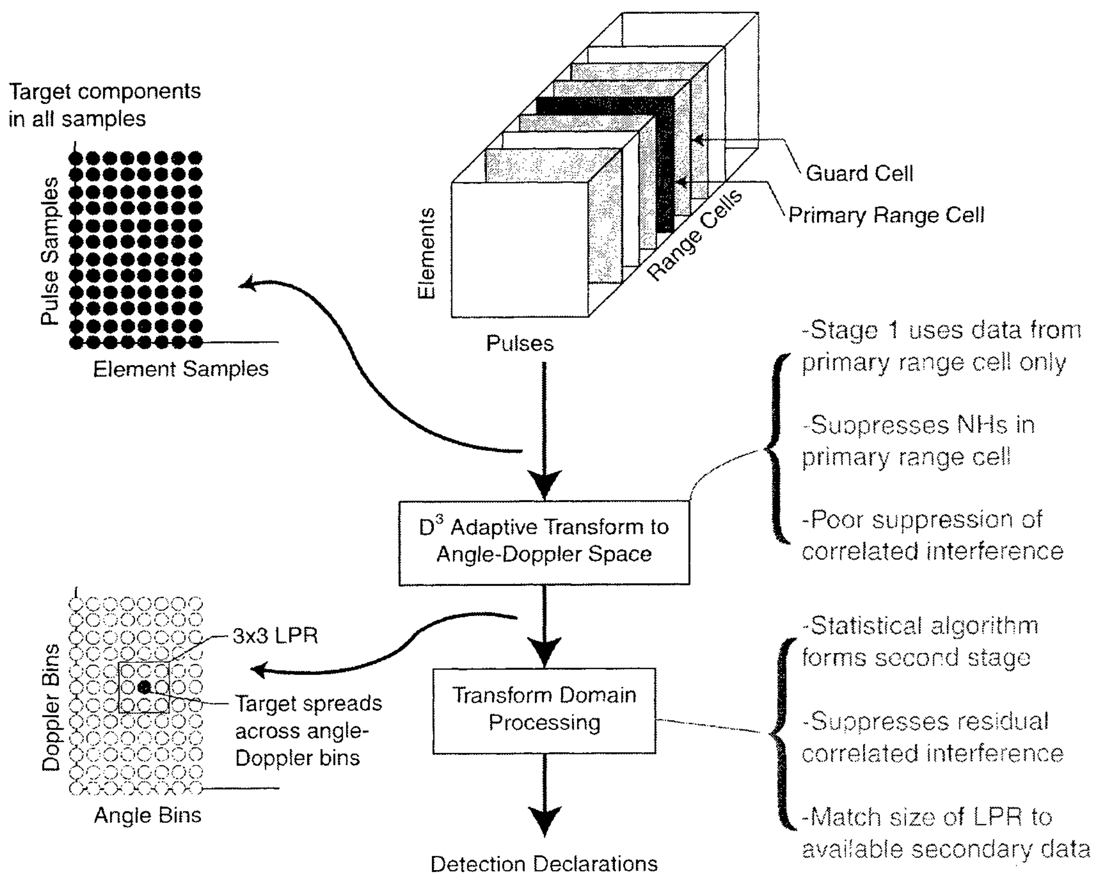

Figure 29: Block diagram of the Two-Stage Hybrid Algorithm

Consider the general framework of any STAP algorithm. The algorithm processes received data to obtain a complex weight vector for each range bin and each look angle/Doppler. The weight vector then multiplies the primary data vector to yield a complex number. The process of obtaining a real scalar from this number for threshold comparison is part of the post-processing and not inherent to the algorithm itself. The adaptive process therefore *estimates the signal component in the look direction* and hence the adaptive weights can be viewed in a role *similar to the non-adaptive steering vectors*, used to transform the space-time data to the angle-Doppler domain.

The JDL processing algorithm begins with a transformation of the data from the space-time domain to the angle-Doppler domain. This is followed by statistical adaptive processing within a LPR in the angle-Doppler domain. The hybrid approach uses the D^3 weights, replacing the non-adaptive steering vectors used earlier. By choosing the set of look angles and Dopplers to form the LPR, the D^3 weights perform a function analogous to the non-adaptive transform. As shown in Figure 29, the D^3 algorithm serves as a first stage *adaptive* transformation from the space-time to the angle-Doppler domain.

JDL statistical processing in the angle-Doppler domain forms the second stage of adaptive processing to filter the residual correlated interference. The D^3 algorithm is used repeatedly with the η_a look angles and the η_d look Doppler frequencies to form the LPR. The space-time data is transformed to the LPR in the angle-Doppler domain using these adaptive weights. Using the D^3 weights from Eqn. (38), the transformation matrix of Eqn. (25) in Section 2.3.2 for $(\phi_{-1}, \phi_0, \phi_1; \eta_a = 3)$ and three Doppler bins $(f_{-1}, f_o, f_1; \eta_d = 3)$ is now given by the $MN \times 9$ matrix

$$\begin{aligned}\mathbf{T} = [\mathbf{w}(\phi_{-1}, f_{-1}) \;\; \mathbf{w}(\phi_{-1}, f_0) \;\; \mathbf{w}(\phi_{-1}, f_1) \\ \mathbf{w}(\phi_0, f_{-1}) \;\; \mathbf{w}(\phi_0, f_0) \;\; \mathbf{w}(\phi_0, f_1) \\ \mathbf{w}(\phi_1, f_{-1}) \;\; \mathbf{w}(\phi_1, f_0) \;\; \mathbf{w}(\phi_1, f_1)]\end{aligned} \tag{39}$$

This adaptive transformation is noninvertible, resulting in some information loss. However, this information loss may be beneficial. The hybrid algorithm takes advantage of this loss to suppress discrete interferers within the range cell of interest. The advantages associated with the JDL algorithm, such as in reduction in the required secondary data support, carry over to the hybrid algorithm.

The same transformation matrix **T** is used to transform the primary and secondary data to the angle-Doppler domain. Furthermore, the steering vector **s** is also transformed to the angle-Doppler domain using this transformation matrix in conjunction with Eqn. (28). Unlike the JDL algorithm, this transformation matrix changes from range cell to range cell. The hybrid algorithm therefore has a significantly higher computation load than the JDL algorithm. The hybrid algorithm forms the adaptive transformation matrix as given by Eqn. (39) for each range cell and then transforms this primary and *associated* secondary data to the angle-Doppler domain. This process is repeated for each range cell.

3.2.2 Example 1: Simulated Data

The first example uses the same data as presented in Section 3.1.1 to illustrate the performance of the D^3 method. There it was shown that the D^3 algorithm can suppress a discrete interference source well, but does not do as well against correlated interference such as white noise jamming and clutter. This example shows the performance of the hybrid algorithm in the same case.

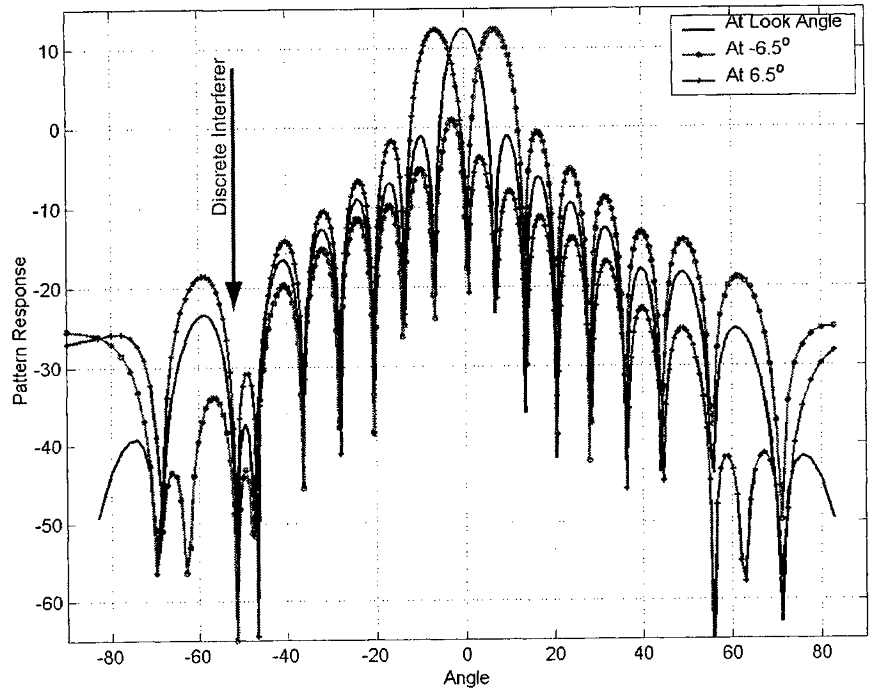

Figure 30: Three D^3 spatial beams used to form LPR

This example uses 3 angle bins and 3 Doppler bins, i.e. a 3×3 LPR. The emphasis parameter κ is chosen to be $(NM)^{1/2}$. Figure 30 plots the spatial beam patterns associated with the three beams used to form the LPR in angle-Doppler domain. Note that the three beams are separated by a chosen beamwidth of 6.5^o. All three patterns show a null in the direction of the discrete interferer at angle -51^o. These beams illustrate the benefits of using the D^3 algorithm as the first stage. The algorithm suppresses discrete interference and the data transformed the angle-Doppler domain is free of the effects of discretes.

Figure 31 plots the antenna beam patterns resulting from the use of the hybrid algorithm. The figure shows that the hybrid algorithm combines the advantages of both statistical and non-statistical adaptive processing. The adapted angle pattern shows deep nulls at -21°, 45°, and -51°, the directions of the two jammers *and the discrete interferer*. Furthermore, the adapted pattern has a deep null at ω=0 resulting in effective nulling of the mainbeam clutter. The hybrid algorithm therefore suppresses correlated interference such as clutter and jamming *and uncorrelated interference such as the strong interferer* in the primary range cell.

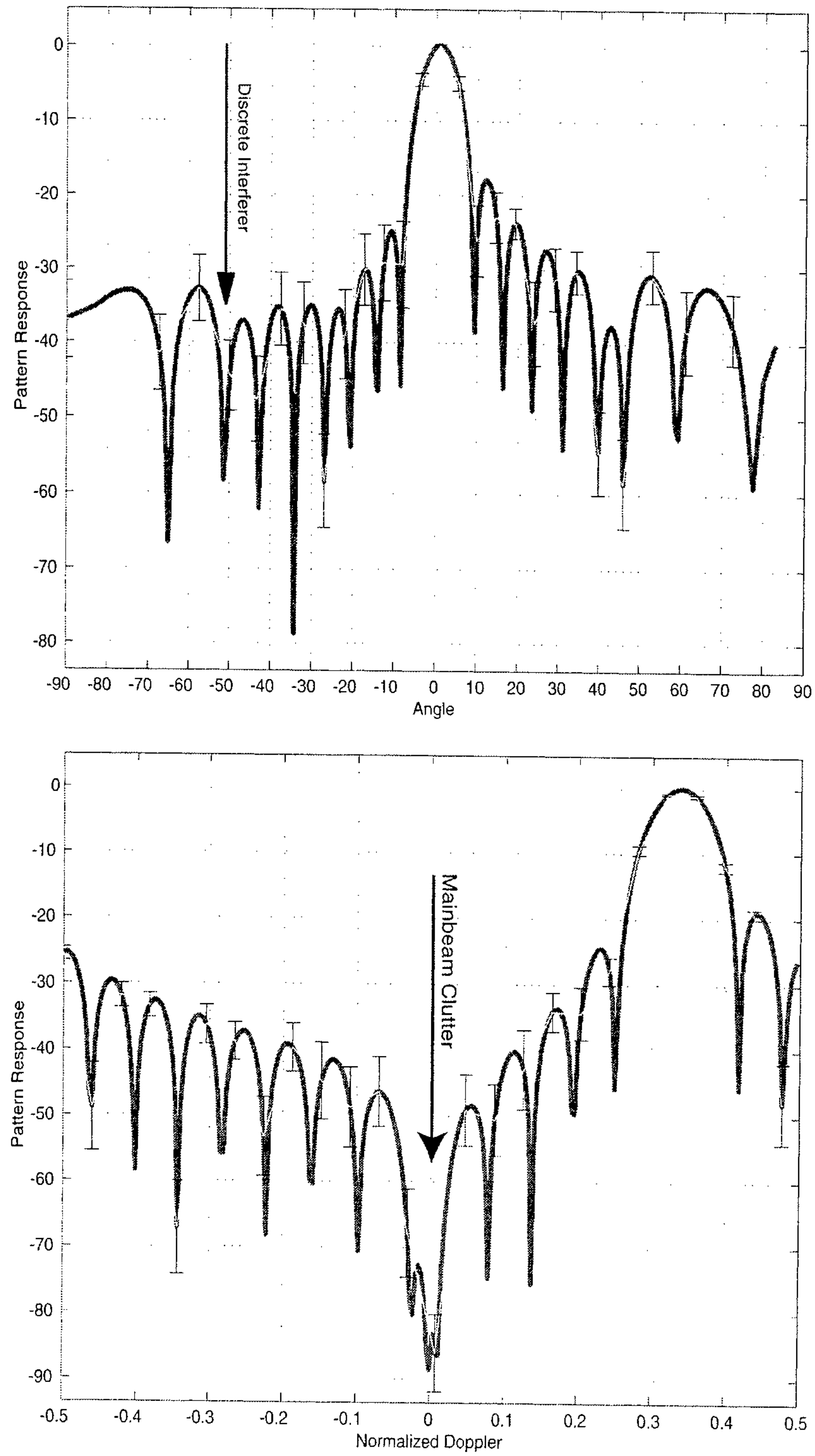

Figure 31: Hybrid Algorithm Patterns at Target Doppler and Azimuth

3.2.3 Applying the Hybrid Algorithm to Measured Data

This section presents two examples of the application of the hybrid algorithm to measured data. The examples use data from the MCARM database. The examples use two acquisitions (acquisitions 575 and 152 on flight 5) to illustrate the suppression of discrete interference in measured data.

Before the hybrid algorithm can be applied to the MCARM database, array effects must be accounted for. The D^3 method was developed in Section 3.1 for an equispaced, linear array of point sensors. This allowed for the assumption of no mutual coupling between the elements and that, for each pulse, the target signal advances from one element to the next by a constant spatial multiplicative factor z_s. This, in turn, allowed for the crucial assumption of the elimination of the target signal in the entries of the interference matrix.

The MCARM antenna is an array of 22 elements arranged in a rectangular 2 x 11 grid. For a rectangular array these assumptions are invalid. Furthermore, as shown in Section 2.2, a real array is affected by mutual coupling and the spatial steering vector must be measured.

Here we compensate for the mutual coupling using the measured steering vectors. Equation (18) indicates that the spatial steering vector at broadside ($\phi = 0$) is given by $\mathbf{a}(\phi = 0)=[1\ 1 \ldots 1\ 1]^T$. In the absence of mutual coupling, this steering vector at broadside is valid for arrays in *any* configuration. The approach then is to artificially rotate all the data, using the measured spatial steering vector, to force the look direction to broadside. This compensates for the rectangular array configuration and the mutual coupling associated with the look direction. The rotation is achieved by an entry-by-entry division of the received voltages at the array level with the measured spatial steering vector corresponding to the look direction. Using pseudo-MATLAB® notation, this operation can be represented by

$$\hat{\mathbf{x}}(m) = \mathbf{x}(m)./\mathbf{a}_m(\phi), \tag{40}$$

where $\mathbf{x}(m)$ represents the N returns from the m^{th} pulse in a CPI and $\mathbf{a}_m(\phi_t)$ represent the measured steering vector corresponding to the look direction ϕ_t. This operation is repeated for all pulses in all range bins.

The division operation of Eqn. (40) forces the effective spatial steering vector for any look direction to be $\mathbf{a}(\phi = 0)=[1\ 1 \ldots 1\ 1]^T$. equivalent to broadside in an ideal array. The hybrid method is applied to the 'rotated' data with broadside as the look direction.

3.2.4 Example 2: Injected Target in MCARM Data

In this example, a discrete non-homogeneity is introduced into the data by adding a strong fictitious target at a single range bin, but not at the look angle-Doppler. Two cases are considered within this example; no injected target and an injected weak target. The first case illustrates the suppression of the discrete non-homogeneity. In the second case, a weak target is injected at the same range bin as the non-homogeneity, but at the look angle and Doppler. This case illustrates the ability of the hybrid algorithm to detect weak targets in the presence of strong discrete non-homogeneities. The data is the same as used earlier in this report to illustrate the performance of the JDL algorithm. In this case, only 22 of the 128 pulses in the CPI are used, i.e. N=22, M=22. The value of the emphasis parameter is $\kappa = (NM)^{3/2}$.

The details of the injected non-homogeneity and weak target are shown in Table 9.

Table 9: Parameters for injected non-homogeneity and target in MCARM Data

Parameter	Non-homogeneity	Target
Amplitude	0.0241	0.000241
Angle bin	35	65 (broadside)
Doppler bin	-3	-2
Range bin	290	290

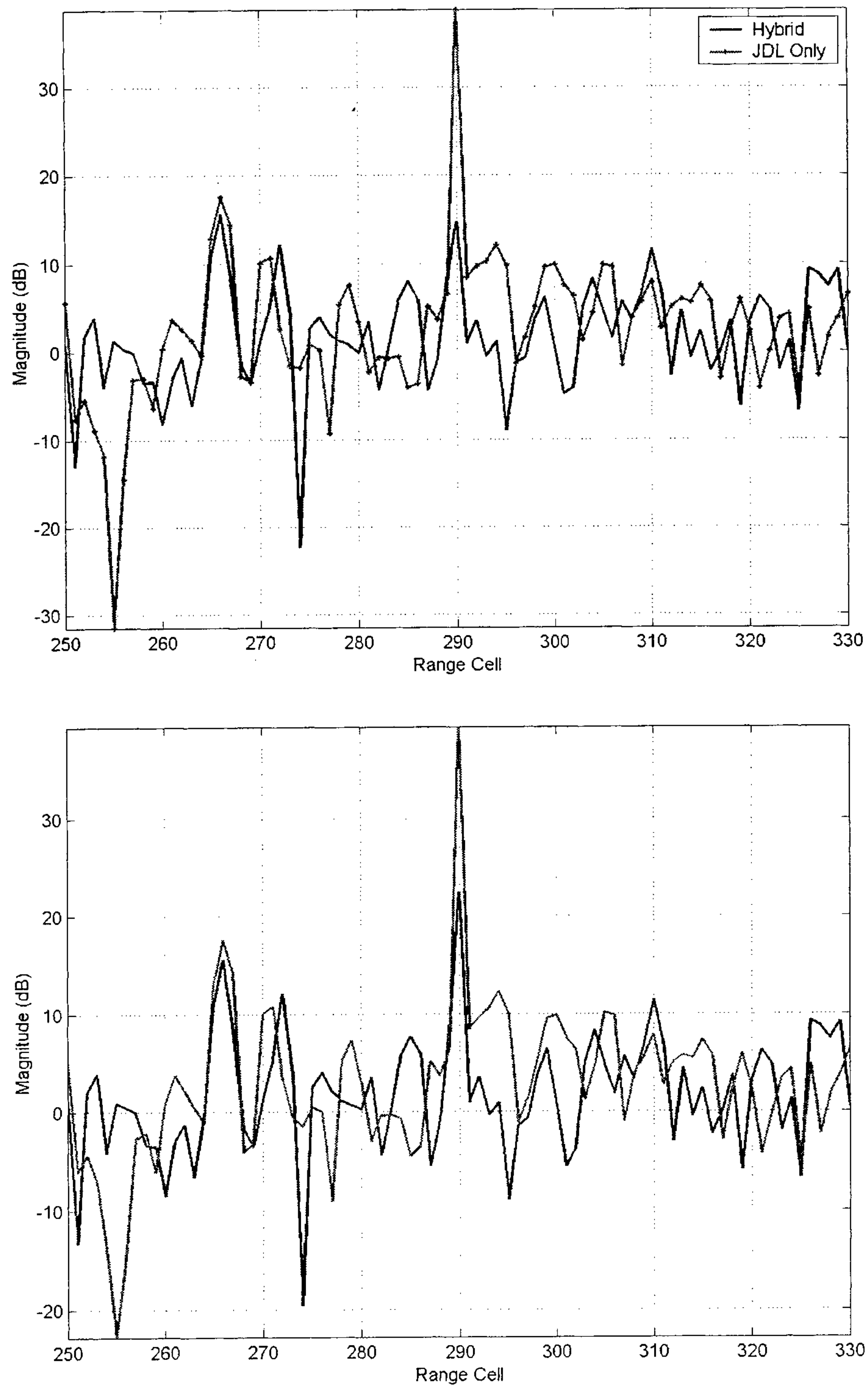

Figure 32: Performance of Hybrid algorithm in countering non-homogeneities: Injected Target (a) With Non-homogeneity, No target (b) With non-homogeneity, With target

The hybrid algorithm is applied to the data from the range bin with the non-homogeneity and surrounding range bins. The output MSMI statistic from the second stage of the hybrid algorithm is plotted as a function of range. In this example, five Doppler bins and five angle bins form the LPR for both the JDL algorithm and the second stage of the hybrid algorithm. One hundred secondary data vectors are used to estimate the 25×25 covariance matrix.

For the case without an injected target, Figure 32(a) compares the output from the JDL algorithm with the output of the hybrid algorithm. As can be seen, the JDL algorithm indicates the presence of a large target in the look direction (angle bin 65). This is because the large non-homogeneity at angle bin 35 and Doppler bin –3 is not suppressed by the statistical algorithm, leading to false alarms at the look direction. On the other hand, the hybrid algorithm shows no target at broadside. The non-homogeneity is suppressed in the first D^3 stage and residual clutter is suppressed in the second JDL stage.

A synthetic target injected at the look direction and Doppler illustrates that sensitivity of the hybrid algorithm to weak targets. The parameters of the weak target are listed in Table 9. Figure 32(b) compares the output of the two algorithms in the case of a strong non-homogeneity and a weak target. The JDL algorithm again shows the presence of a strong target in the look direction. However, from Figure 32(a), we know that the strength of the statistic is caused by the non-homogeneity. On the other hand, the plot for thee hybrid algorithm shows the statistic at the target range bin is 6.9 dB above the next highest peak.

This example shows that the hybrid algorithm may be use to detect a weak target in the presence of a discrete non-homogeneity within the range cell of interest.

3.2.5 Example 3: MTS Tones in the MCARM Data:

Certain acquisitions within the MCARM database include signals from a moving target simulator (MTS) at known Doppler shifts. This acquisition was used in Section 2.3.4.2 to illustrate the benefits of accounting for array effects. In acquisition 152 on flight 5, the MTS tones occur in angle bin 59. In this example, the look direction is set to angle bin 85 for a mismatch and the JDL and hybrid algorithms are applied to the same acquisition. For this look direction, the MTS tones at angle bin 59 act as strong targets at a different angle bin, i.e. discrete non-homogeneities. As in Example 1, two cases are considered; no injected target and a weak injected target. The first case illustrates the suppression of the MTS tones acting as discrete, strong non-homogeneities. The second case illustrates the sensitivity of the hybrid algorithm to weak targets. This example uses all 128 pulses in the CPI, i.e. $N = 22$, $M = 128$. The emphasis parameter for the direct data domain method is set to a large value of $\kappa = (NM)^{3/2}$.

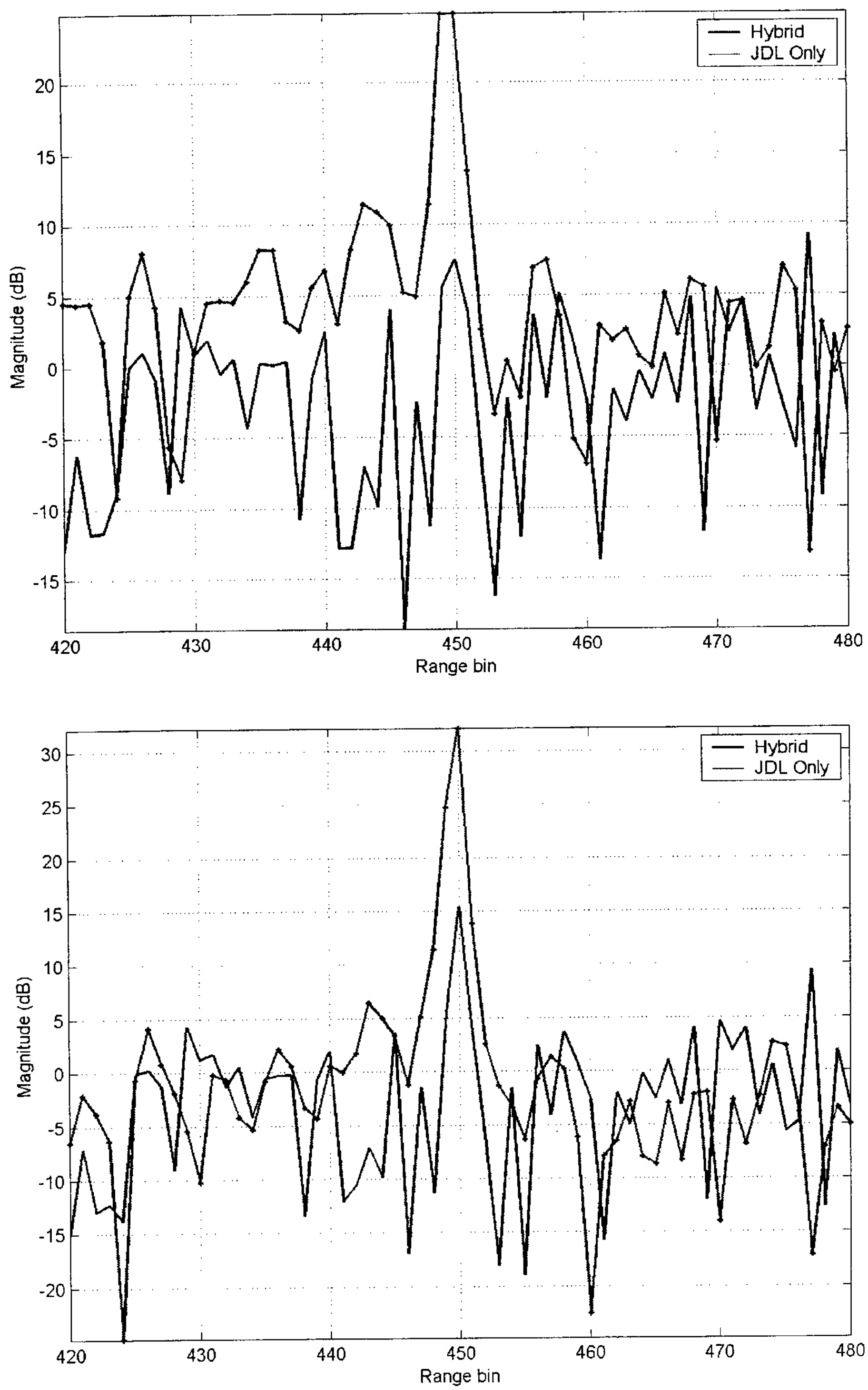

Figure 33: Performance of Hybrid algorithm in countering non-homogeneities: MTS Data (a) With Non-homogeneity, No target (b) With non-homogeneity, With target

In this acquisition, the MTS tones are in range bin 449-450 with the strongest tone at a Doppler corresponding to bin –53 and angle bin 59. The example focuses on the suppression of this tone. Figure 33(a) plots the MSMI statistic of the two algorithms for the case without any artificial injected targets. The JDL algorithm detects a large target at range bins 449 and 450. This false alarm is due to the strong MTS tone at angle bin 59 even though the look direction is set at angle bin 85. The hybrid algorithm, however, suppresses the strong MTS tone, showing no activity at range bins 449 and 450.

Figure 33(b) plots the results of using the two algorithms to detect a weak target injected into range bin 450. The parameters of the weak target are; magnitude: 0.0001, Doppler bin: -53, angle bin: 85. This weak target is easily detected by the hybrid algorithm with the statistic at the target range bin 9.8 dB above the next highest peak.

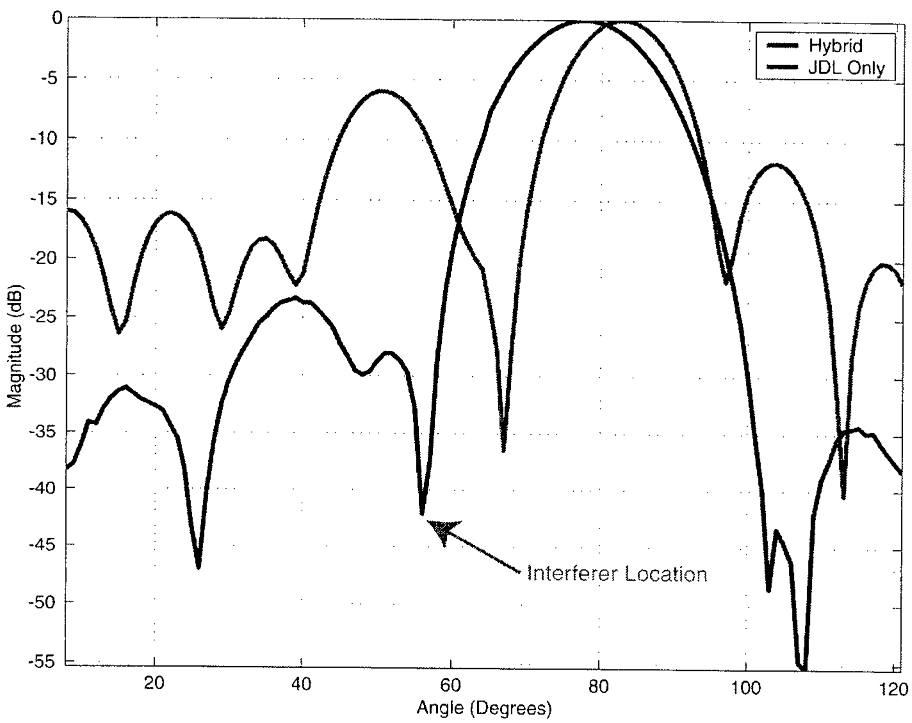

Figure 34: Beam Pattern associated with the Hybrid and JDL methods

The beam patterns associated with the two algorithms illustrate the improvement in using the D^3 algorithm as the first stage of a two-stage hybrid method. Figure 34 plots the spatially adapted beam pattern at the look Doppler frequency for the JDL and hybrid algorithms. The plot for the hybrid algorithm shows the deep null in the adapted pattern of the hybrid algorithm near angle bin 59 while the JDL pattern does not show such a null. In applying the JDL algorithm to the MCARM data acquisition with MTS tones, the strong tones leak through the sidelobes of the adapted pattern, leading to false alarms.

4.0 Conclusions

The theme of this effort has been the development of the theoretical foundations to move space-time adaptive processing from theory to practice. Two aspects of this problem were investigated in considerable detail: mutual coupling and non-homogeneous data. The impact of mutual coupling has been investigated for direct data domain and the statistical joint domain localized processing algorithm. To counter the impact of non-homogeneous data this effort developed a new two dimensional D^3 algorithm. This algorithm is then extended to a radically new hybrid algorithm that combines non-statistical D^3 processing with statistical JDL processing.

In developing array signal processing concepts, researchers have usually ignored the fact that the antenna array is itself a complex electromagnetic system. Here a detailed numerical analysis is used to demonstrate that, if not accounted for, electromagnetic phenomena severely degrade the performance of STAP algorithms. The key contribution of this research was to show that effective compensation for these effects requires a *detailed* numerical analysis, such as the Method of Moments. Earlier approaches are only valid in relatively low-interference environments. This effort was the first to use such a detailed analysis *and the formulation provides far superior compensation for electromagnetic effects than the earlier open-circuit model.* In addition, the compensation procedure is reduced to a pre-multiplication with a matrix, i.e. the procedure does not place a heavy real time computation load.

Joint Domain Localized (JDL) processing is a popular Space-Time Adaptive Processing (STAP) algorithm where adaptive processing occurs after transformation of the space-time data to the angle-Doppler domain. This algorithm was originally developed for an ideal array of point sensors, ignoring the electromagnetic effects in a real antenna array. The transformation is then equivalent to a 2D FFT. The performance of this algorithm degrades when using real arrays and measured data. To compensate, under this effort we introduce the use of a *transformation matrix*, based on measured steering vectors, an approach valid for both ideal and real antenna arrays. The use of such a matrix transform accounts for the correlation between the non-orthogonal *measured* steering vectors. This formulation also removes other restrictions due to the use of the 2D FFT. The use of the appropriate transformation matrix improves performance by *an average of 7dB in testing using measured data.*

Traditional statistical STAP algorithms assume the interference to be homogeneous and that the interference covariance matrix is estimated by averaging over several received data samples. However, in the real world, interference is non-homogeneous (non-stationary) and the performance of purely statistical algorithms degrades. This effort introduced a new *hybrid* algorithm that builds on earlier attempts at non-statistical processing in non-homogeneous data. The hybrid approach treats the non-statistical approach as an *adaptive transform* to angle-Doppler space. JDL-like statistical processing in the angle-Doppler domain then forms the second stage. The algorithm uses the transformation matrix formulation introduced under this effort with the matrix now representing the adaptive transformation. For the first time a practical algorithm that combines the benefits of statistical and non-statistical processing has been developed. This algorithm is applicable in non-homogeneous scenarios.

In summary, the issues raised in this effort are important to fielding STAP algorithms in fielded airborne radar systems. This research has developed practical techniques to deal with two important real world phenomena: mutual coupling and non-homogeneous data.

5.0 References

[1] R.A. Monzingo, T.W. Miller, *Introduction to Adaptive Arrays*. 1980: Wiley Interscience.

[2] L.E. Brennan, I.S. Reed, "Theory of adaptive radar". *IEEE Transactions on Aerospace and Electronic Systems,*. vol. 9 no. 3, July 1973: pp. 237-252 .

[3] I.S. Reed, J.D. Mallet, L.E. Brennan, "Rapid convergence rate in adaptive radars". *IEEE Transactions on Aerospace and Electronic Systems,*. vol. 10 no. 6, November 1974: pp. 853-863 .

[4] J. Ward, *Space-time adaptive processing for airborne radar*, F19628-95-C-0002, MIT Lincoln Laboratory, Cambridge, MA, 1994.

[5] H. Wang, L. Cai, "On adaptive spatial-temporal processing for airborne surveillance radar systems". *IEEE Transactions on Aerospace and Electronic Systems,*. vol. 30 no. 3, July 1994: pp. 660-669 .

[6] T.K. Sarkar, N. Sangruji, "An adaptive nulling system for a narrow band signal with a look direction constraint utilizing the conjugate gradient method". *IEEE Transactions on Antennas and Propagation,*. vol. 37 no. 7, July 1989: pp. 940-944 .

[7] R. Schneible, *"A Deterministic Least Squares Approach to STAP"*, Department of Electrical Engineering, 1996, Syracuse University: Syracuse, NY.

[8] I.J. Gupta, A.A. Ksienski, "Effect of mutual coupling on the performance of adaptive arrays". *IEEE Transactions on Antennas and Propagation,*. vol. 31 no. September 1982: pp. 549-553 .

[9] R.S. Adve, T.B. Hale, M.C. Wicks, "Joint Domain Localized adaptive processing in homogeneous and non-homogeneous Environments. Part I: Homogeneous Environments". *IEE Proc. on Radar, Sonar and Navigation,*. vol. 147 no. 2, April 2000: pp. 57-65 .

[10] R.S. Adve, T. K. Sarkar, "Compensation for the effects of mutual coupling on direct data domain algorithms". *IEEE Transactions on Antennas and Propagation,*. vol. 48 no. 1, January 2000: pp. 86-94 .

[11] S.A. Schelkunoff, H.T. Friis, *Antenna Theory and Practice*. 1966, New York: Wiley Publishing.

[12] R.F. Harrington, *Field Computation by Moment Methods*. 1982: Robert E. Kreiger Publishing Co.

[13] B. Himed, *"Application of Matrix Pencil approach to direction finding"*, Electrical and Computer Engineering, 1990, Syracuse University: Syracuse.

[14] H. Steyskal, J.S. Herd, "Mutual coupling compensation in small array antennas". *IEEE Transactions on Antennas and Propagation*,. vol. 38 no. 12, December 1990: pp. 1971-1975 .

[15] C.C. Yeh, M.L. Leou, D.R. Ucci, "Bearing estimations with mutual coupling". *IEEE Transactions on Antennas and Propagation*,. vol. 37 no. 10, October 1989: pp. 1332-1335 .

[16] B.J. Strait, T.K. Sarkar, D.C.Kuo, *Special Programs for analysis of radiation by wire antennas*, Technical Report AFCRL-TR-73-0399, Syracuse University, June 1973.

[17] A.R. Djordjevic, et.al., *Analysis of Wire Antennas and Scatterers: Software and User's Manual*. 1995: Artech House.

[18] W.L. Melvin and B. Himed, "Comparative analysis of space-time adaptive algorithms with measured airborne data", Proceedings of the 7th International Conference on Signal Processing Applications & Technology, October 1996.

* [19] D. Sloper, D. Fenner, J. Arntz and E. Fogle, "Multi-channel airborne radar measurement (MCARM) flight test", Final report, contract F30602-92-C-0161, Westinghouse Electronic Systems, April 1996. Additional information available at *http://sunrise.deepthought.rl.af.mil*. RL-TR-96-49

* [20] A. Jaffer, W. Baker, W. Ballance and J. Staub "Adaptive space-time processing techniques for airborne radars", Contract F30602-89-D-0028, Hughes Aircraft Company, Fullerton, CA 92634, July 1991. RL-TR-91-162

[21] F. Harris, "On the use of windows for harmonic analysis with the Discrete Fourier Transform", *Proc. of the IEEE*, vol. 66, No. 1, pp. 51-83, Jan. 1978

[22] H.H. Chang, "*Improving Space-Time Adaptive Processing (STAP) Performance in Nonhomogeneous Clutter*", Ph.D. thesis, Syracuse University, August 1997.

[23] R.S. Adve, T.B. Hale and M.C. Wicks, "Joint Domain Localized Adaptive Processing in Homogeneous and Non-homogeneous Environments. Part II: Non-Homogeneous Environments", *IEE Proc. on Radar, Sonar and Navigation* vol. 147, no. 2, pp. 67-74, April 2000.

*RL-TR-96-49 is Distribution authorized to DoD and DoD contractors only; Critical Technology.
*RL-TR-91-162 is Distribution authorized to U.S. Gov't agencies and their contractors; Critical Technology

☆U.S. GOVERNMENT PRINTING OFFICE: 2001-610-055-10153